energies

MDPI

Article

Effects Analysis of FAME on the Engine Characteristics of Different Polymerized Biofuels in Compression Ignition Engine

Hongting Zhao [1,2], Zhiqing Zhang [1,2,*], Kai Lu [2], Yanshuai Ye [1] and Sheng Gao [1]

[1] Guangxi Earthmoving Machinery Collaborative Innovation Center, Guangxi University of Science and Technology, Liuzhou 545006, China; 202200206033@stdmail.gxust.edu.cn (H.Z.); yeyanshuai@gxust.edu.cn (Y.Y.); 221068137@stdmail.gxust.edu.cn (S.G.)

[2] School of Mechanical and Automotive Engineering, Guangxi University of Science and Technology, Liuzhou 545006, China; 20230102022@stdmail.gxust.edu.cn

* Correspondence: zhangzhiqing@gxust.edu.cn

Abstract: Environmental pollution caused by marine engines fueled with fossil fuels is a matter of growing significance. The search for renewable and clean energy sources and improvements in the way fossil fuels are burnt aims to reduce the environmental impact of these engines. For this purpose, fatty acid methyl esters were produced from pure canola oil using KOH-assisted methanol-based transesterification with a maximum yield of 90.68 ± 1.6%. The marine engine's model was created with CONVERGE software, followed by experimental verification. This paper examines the blended fuel characteristics of a diesel engine with biodiesel blends (0%, 5%, 10%, and 15%) at different loads of engines (50%, 75%, and 100%). It also explores the variation in these characteristics of B10 (10% biodiesel–diesel blends) at three different load conditions and four different EGR rates (0%, 5%, 10%, and 15%). The results indicate that the addition of biodiesel to diesel fuel reduces CO, HC, and soot emissions, while increasing NO_x emissions. Additionally, the EGR rate decreases NO_x emissions but results in higher levels of soot, CO, and HC emissions. Finally, response surface methodology was used to elicit the engine's characteristics. It was determined that the optimum experimental operating conditions were 100% engine load, 6.9% biodiesel addition, and 7.7% EGR. The corresponding BTE, BSFC, NO_x, and HC emissions were 38.15%, 282.62 g/(kW-h), 274.38 ppm, and 410.37 ppm, respectively.

Keywords: diesel-biodiesel blended fuel; fatty acid methyl esters; marine engine; RSM

Citation: Zhao, H.; Zhang, Z.; Lu, K.; Ye, Y.; Gao, S. Effects Analysis of FAME on the Engine Characteristics of Different Polymerized Biofuels in Compression Ignition Engine. *Energies* **2024**, *17*, 2255. https://doi.org/10.3390/en17102255

Academic Editor: Diego Luna

Received: 14 April 2024
Revised: 30 April 2024
Accepted: 3 May 2024
Published: 8 May 2024

1. Introduction

In the face of escalating environmental pollution and the dwindling supply of non-renewable energy sources [1], there has been a heightened emphasis on environmental pollution control. However, with ongoing increases in the global population, technological advancements, and industrial development, human demand for energy is on the rise [2]. The engine cylinder combustion of non-renewable fossil fuels leads to the emission of pollutants including soot, CO, HC, and NO_x [3], prompting the search for renewable and environmentally friendly alternatives. One such alternative that has garnered significant attention is biodiesel [4].

Biodiesel is a renewable fuel devoid of polycyclic aromatic compounds [5], primarily sourced from natural animal and plant oils [6]. It can be classified into various types, including plant synthesis, animal synthesis, microbial synthesis, blended synthesis, plant oil purification, and animal oil purification [7]. While the sources of plant oils for biodiesel production are diverse, oilseed crops are commonly utilized, with canola oil being one of the principal raw materials for the production of biodiesel [7]. Plant oils are often processed into biodiesel via esterification reactions, which are considered to be one of the most promising methods due to their low cost and simplicity of operation [8]. Therefore, in this study, canola oil was selected as the feedstock, and methanol catalyzed by KOH was

used for the transesterification reaction to produce FAME. The reaction parameters of the transesterification reaction were optimized using the single variable method [9].

The advantages of biodiesel application in diesel engines are evident, as follows: (1) Biodiesel exhibits similar physical and chemical properties to diesel, enabling direct blending with diesel in any proportion without requiring modifications to fuel supply and injection systems, thus allowing its direct application in diesel engines [10]. It maintains nearly identical brake thermal efficiency, BSFC, and brake power [11]. (2) Biodiesel has a higher cetane number and oxygen content than diesel [12], with an oxygen content of approximately 10–11%, and it is free from sulfur and polycyclic aromatic compounds [5]. These characteristics of biodiesel facilitate thorough combustion in the engine, significantly reducing emissions of toxic pollutants such as CO and soot [13]. (3) Biodiesel exhibits good lubricating properties. Its dynamic viscosity is higher than that of traditional fossil diesel, resulting in better lubrication performance. This reduces friction losses during engine operation, leading to smoother engine operation and increased engine lifespan [14]. (4) Biodiesel has a higher flash point and cloud point, indicating lower susceptibility to explosion. Therefore, biodiesel is safer than conventional diesel in terms of transportation, storage, and utilization [12]. However, due to biodiesel's poor low-temperature flow properties and oxidative stability, as well as its corrosiveness, its use may lead to corrosion and damage to rubber components and metal hoses in the fuel supply system [15]. Moreover, the poor low-temperature flow properties and oxidative stability further limit the standalone use of biodiesel in diesel engines, necessitating the blending of biodiesel with a certain proportion of diesel or other fuels capable of improving its cold flow and oxidative characteristics for practical use [16].

In diesel engines, numerous researchers have explored the utilization of biodiesel. José et al. [17] discovered that biodiesel enhanced the combustion characteristics of diesel engines, resulting in decreased emissions of soot, HC, and CO. Karavalakis et al. [18] examined the application of low-concentration biodiesel–diesel blends in a heavy-duty diesel engine, revealing that high-saturation biodiesel blends did not increase NO_x emissions. Additionally, both high- and low-saturation biodiesel blends showed an overall decrease in HC and CO emissions in most testing cycles. Yoon and his team [19] conducted experiments and found that the addition of canola oil biodiesel slightly reduced combustion pressure and indicated mean effective pressure at low speeds, while showing a slight increase at medium speeds. Uyumaz et al. [20] blended diesel with poppy seed oil biodiesel and observed that biodiesel blending prolonged the combustion delay period, with thermal efficiency decreasing by 5.73% and 13.05% for 10% and 20% biodiesel blend ratios, respectively.

To reduce emissions of pollutants, considerations extend beyond fuel properties to include technological advancements [21]. For diesel engines, extensive research has indicated that EGR technology is one of the most common methods used to reduce the mean emissions of pollutants [22]. NO_x is primarily produced in high temperature, high oxygen conditions, and EGR can decrease the combustion chamber temperature and NO_x emissions [23]. Hitoshi Yokomura [24] explored the influence of EGR rates on engine combustion characteristics, revealing that higher EGR rates and excess air ratios successfully reduced NO_x emissions. Kumar [25] and Saravanan [26] investigated the impact of EGR rates on diesel engines, demonstrating that increasing EGR rates could reduce NO_x emissions. Furthermore, research by Dickey et al. [27] indicated that the emission of NO_x could be reduced by over 50% with an EGR rate of 15%, and over 80% with an EGR rate of 25%. However, increasing EGR could increase the emissions of PM and HC.

In summary, while biodiesel offers significant advantages in reducing soot, CO, and HC emissions in exhaust gases [28], it can increase the emission of NO_x within the cylinder. NO_x and particulate matter can be reduced by utilizing EGR technology. Therefore, in order to improve the combustion and emission of diesel engines, this study employed CFD software coupled with chemical reaction kinetics to simulate and investigate the effects of three loads (50%, 75%, and 100%), four biodiesel–diesel blend ratios, and four EGR rates on

the combustion, performance, and emission characteristics of marine engines. RSM was utilized to optimize dual-fuel engines to maximize BTE and minimize BSFC, NO_x, HC, and CO emissions.

2. Materials and Methods

This section focuses on the modeling and validation of fuel engines. CONVERGE Studio v3.0 simulation software was used to determine the combustion characteristics and emission characteristics. The combustion characteristics included in-cylinder pressure and in-cylinder combustion temperature, and the emission characteristics included soot, NO_x, CO, and HC emissions. The AVL-BOOST 2020 R1 software determined the performance characteristics, including fuel consumption and thermal efficiency. Table 1 presents the theoretical models involved in this study.

Table 1. The sub-models selected [27–35].

Model	Selected Models
Spray-wall interaction model	Rebound/slide model
Evaporation model	Frossling drop evaporation model
Emission model	Hiroyasu-NSC soot model and extended Zeldovich NO_x model
Turbulent diffusion model	O'Rourke model
Turbulence model	RNG k-ε model
Combustion model	SAGE model
Spray breakup model	KH-RT model

2.1. Fundamental Equations

2.1.1. Fundamental Governing Equations

In 3D numerical simulations, the diesel engine obeys the equations of mass conservation, energy conservation, momentum conservation, and species conservation. The basic system of the equations is as follows:

$$\frac{\mathrm{d}m}{\mathrm{d}t} = \sum_{bounds} m_\mathrm{f} \tag{1}$$

$$\frac{\mathrm{d}(\rho HV)}{\mathrm{d}t} = V\frac{\mathrm{d}p}{\mathrm{d}t} - hA_\mathrm{S}(T_\mathrm{fluid} - T_\mathrm{wall}) + \sum_{bounds}(m_\mathrm{f} \cdot H) \tag{2}$$

$$\frac{\mathrm{d}(m_\mathrm{flx})}{\mathrm{d}t} = \frac{\sum_{bounds}(m_\mathrm{f} \cdot u) - 4C_\mathrm{f}\frac{\mathrm{d}x\mathrm{A_s}}{\Phi}\frac{\rho u^2}{2} - C_\mathrm{p}(\frac{1}{2}\rho u^2)\mathrm{A_s} + \mathrm{d}p\mathrm{A_s}}{\mathrm{d}x} \tag{3}$$

$$\rho\left(\frac{\partial Y_i}{\partial_t} + \frac{\partial Y_i}{\partial_x} + \frac{\partial Y_i}{\partial_y} + \frac{\partial Y_i}{\partial_z}\right) + \frac{\partial}{\partial_x}(\rho Y_i V_{ix}) + \frac{\partial}{\partial_y}(\rho Y_i V_{iy}) + \frac{\partial}{\partial_z}(\rho Y_i V_{iz}) = \varpi_n \tag{4}$$

where m is the volumetric flow rate, m^3/s; C_p is the loss coefficient; A is the cross-sectional area of the fluid, cm^2; C_f is the friction coefficient; u is the boundary velocity, m/s; T_wal is the wall temperature, K; ρ is density, $\mathrm{g/cm}^3$; T_fuel is the fluid temperature, K; h is the heat transfer coefficient, $\mathrm{W/(m^2 \cdot K)}$; Φ is the equivalent diameter, mm; H is total enthalpy, kJ; A_s is the heat transfer area, cm^2; p is pressure, Pa; V is volume, m^3; m_f is the mass flow rate, kg/s; and Y_i is the mass fraction of the i species.

2.1.2. Turbulence Simulation

Turbulent motion significantly affects gas formation, flame propagation, and combustion product formation. The k-ε model is considered to possess a high degree of accuracy

as well as feasibility [29]. Therefore, the k-ε model was chosen to simulate the turbulence within the cylinder. Its dissipation transport is defined by the equation:

$$\begin{aligned}\rho\left(\frac{\partial \varepsilon}{\partial t}+\frac{\partial\left(\mu_{\mathrm{i}} \varepsilon\right)}{\partial x_{\mathrm{i}}}\right) &= \frac{\partial}{\partial x_j}\left(\frac{\mu}{\mathrm{Pr}_\varepsilon} \frac{\partial \varepsilon}{\partial x_{\mathrm{j}}}\right)-c_{\varepsilon_3} \rho \varepsilon \frac{\partial u_{\mathrm{i}}}{\partial x_{\mathrm{i}}} \\ &+\left(c_{\varepsilon_1} \frac{\partial u_{\mathrm{i}}}{\partial x_{\mathrm{j}}} \sigma_{\mathrm{ij}}-c_{\varepsilon_2} \rho \varepsilon+c_{\mathrm{s}} S_{\mathrm{s}}\right) \frac{\varepsilon}{k}-\rho R\end{aligned} \tag{5}$$

where S represents the source term; σ_{ij} is the stress tensor, N/m; and μ_{i} is the turbulent viscosity, cPs/40 °C.

2.1.3. Liquid Droplet Breakup Model

For blended diesel fuel, the atomization phenomenon and droplet breakup state are commonly modeled using the KH–RT model [30]. Therefore, in this study, the KH–RT model was adopted as the droplet breakup model.

In the CONVERGE software, the KH model accurately simulates the process of droplet fragmentation under high density and high relative velocity conditions. The RT model predicts the occurrence of unstable RT waves caused by the sudden deceleration of droplets. In addition, the KH and RT models were combined in an integrated KH–RT model [31].

According to the surface wave theory, the radius of the daughter droplet r_s can be expressed as:

$$r_s = B_0 \Lambda_{\mathrm{KH}} \tag{6}$$

where r_{s} is the new diameter at which the droplet breaks up and reaches a steady state, μm; B_0 is a constant, and in this study, was taken as 0.61; and Λ_{KH} is the wavelength of the unstable surface wave, μm.

The rate of change in the droplet radius and the break-up time are determined as follows:

$$\frac{\mathrm{d}r_s}{\mathrm{d}t} = \frac{\left(r_s - r_p\right)}{\Gamma_{KH}}, \left(r_s \geq r_p\right) \tag{7}$$

$$\Gamma_{KH} = \frac{3.726 B_1 r_p}{\Omega_{KH} \Lambda_{KH}} \tag{8}$$

$$\frac{\Lambda_{\mathrm{KH}}}{r_{\mathrm{p}}} = 9.02 \frac{\left(1+0.4 T_0^{0.7}\right)\left(1+0.45 Z_0^{0.5}\right)}{\left(1+0.87 We_{\mathrm{g}}^{1.67}\right)} \tag{9}$$

$$\Omega_{KH}\left[\frac{\rho_l r_p^3}{\sigma}\right]^{-0.5} = \frac{\left(0.38 We_g^{1.5}+0.34\right)}{\left(1+1.4 T_0^{0.6}\right)\left(1+Z_l\right)} \tag{10}$$

where r_{p} is the original droplet diameter, μm; and B_1 is a constant related to the initial perturbation of the liquid jet, s.

2.1.4. Liquid Density

Using the following formula, the liquid density can be calculated:

$$\left(1-T_{\text{R-T}}\right)^{2/7} = \left(1-\frac{T}{T_{\mathrm{b}}}\right)^{2/7} - \phi \tag{11}$$

$$V_{\mathrm{S}} = V_{\text{S-R}} Z_{\mathrm{Ra}}^{\mathrm{f}} \tag{12}$$

$$\rho = \frac{\rho_R}{Z_{\mathrm{Ra}}^{\mathrm{f}}} \tag{13}$$

where $T_{\text{R-r}}$ and $V_{\text{S-r}}$ are the temperature and density variations at the reference temperature, respectively.

2.1.5. Emission Model

In general, combustion in dual-fuel engines generates a significant amount of NO_x emissions, with the majority being NO [32]. This paper selected the extended Zeldovich model. The following three reactions were considered:

$$N_2 + O \underset{K_1^-}{\overset{K_1^+}{\longleftrightarrow}} NO + N \quad (14)$$

$$O_2 + N \underset{K_2^-}{\overset{K_2^+}{\longleftrightarrow}} NO + O \quad (15)$$

$$N + OH \underset{K_3^-}{\overset{K_3^+}{\longleftrightarrow}} NO + H \quad (16)$$

Soot is a form of carbon particle with a diameter ranging from 0.1 to 10 μm, typically produced by incomplete combustion in high-temperature, high-pressure, and oxygen-deficient conditions in dual-fuel engines [33]. The soot model in this paper utilized the Kinetic model built into the CONVERGE.

2.2. Boundary Conditions

To save computational time, this study did not consider the intake and exhaust processes. The calculation time was set to start at the closure of the intake valve, and end when the exhaust valve opened. The boundary conditions were set based on experimental data provided by the 4190Z engine model [34]. The manufacturer of this equipment is CNPC Jichai Power Company Limited in Jinan, Shandong province, China. The computational area of the one-eighth engine model sketch is shown in Figure 1. This study modeled one-eighth of the combustion chamber due to the symmetrical bowl structure. The specifications are shown in Table 2.

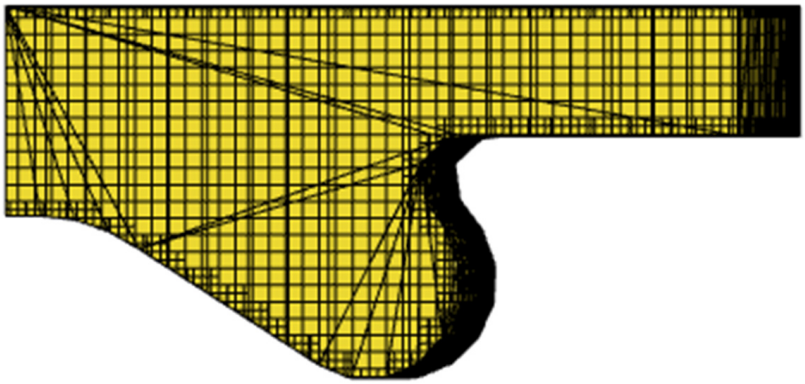

Figure 1. CFD model.

Table 2. Engine boundary conditions.

Type	Value	Type	Value
Stroke × Bore (mm)	210 × 190	The initial turbulent kinetic energy (m^2/s^2)	18.46
Connecting rod (mm)	410	Fuel injection pressure (MPa)	81.12
Rate speed (r/min)	1000	Inlet pressure (MPa)	0.189
Number of cylinders	4	Initial inlet temperature (K)	312.26
Effective power (kW)	220	Piston top temperature (K)	626.12
Number of nozzles	8	Cylinder head surface temperature (K)	552.18
Nozzle radius (mm)	0.3	Compression ratio (-)	14

2.3. Mesh Generation

Based on experimental conditions, this paper conducted a comparative analysis of cylinder pressure during the combustion process of biodiesel–diesel blend fuel to validate the applicability of the model. Corresponding dynamic meshes were developed based on the geometric shape of the dual-fuel engine, establishing an eighth-piston model with an injection cone angle of 150°. However, excessively fine meshes during modeling can significantly increase simulation computation time. As shown in Figure 2, the cylinder pressures were under three different mesh sizes for the dual-fuel engine. When selecting 1.4 mm and 2 mm mesh sizes, their cylinder pressures were essentially the same. Therefore, this paper chose a 2 mm mesh for its simulation studies, which not only ensured computational accuracy, but also significantly reduced computation time.

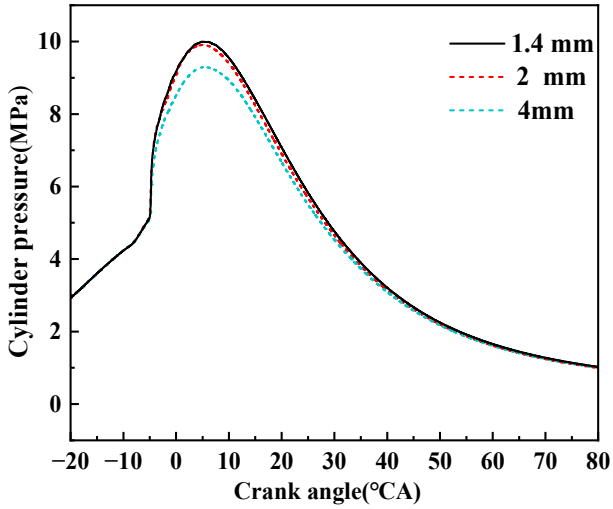

Figure 2. Mesh independence.

2.4. Dual-Fuel Engine Configuration

2.4.1. Fuel Characteristics

The methodology and physicochemical properties of the transesterification reaction have been described in detail in previous papers published by our team [35,36] and will not be described here. FAME was produced by the transesterification reaction of rapeseed oil with methanol using 1% wt/wt potassium hydroxide as the basic catalyst, a methanol-oil molar ratio of 6:1, and a reaction time of 1 h. The main physical and chemical properties of the experimental fuels are shown in Table 3.

Table 3. Fuel properties.

Fuel	Heating Value (MJ/kg)	Viscosity (cPs/40 °C)	Density (g/m^3/15 °C)	Oxygen Content (wt%)
D100	42.7	2.75	0.844	0.3
B5	42.54	2.89	0.846	0.38
B10	42.38	3.07	0.848	0.46
B15	42.25	3.16	0.849	0.53
B100	39.53	4.45	0.882	10.7

2.4.2. Diesel Engine Specifications

The experiment was conducted on a dual-fuel engine, as depicted in Figure 3. Different blending ratios were injected into the cylinder through injectors. A magnetic fuel flow sensor was used to measure fuel flow rate, an electronic fuel pressure sensor was used to measure fuel pressure, and a thermocouple-type fuel temperature sensor was used to measure fuel temperature during the experiment.

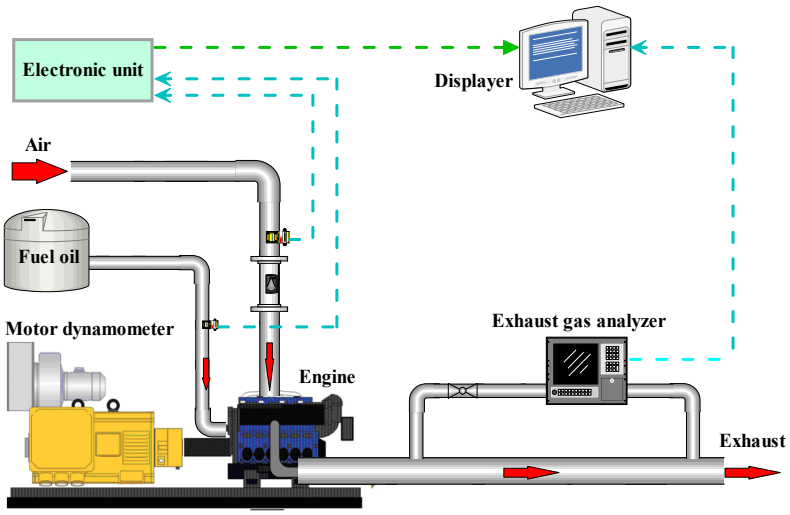

Figure 3. Experimental flow chart.

2.4.3. Feasibility Testing and Model Validation

As shown in Figure 4, the simulated cylinder pressure was lower than the experimental results by approximately 0.08, −0.16, and −0.21 MPa. The heat release rates at different loads showed differences between experimental and simulated values within an acceptable range. Furthermore, the comparison of NO_x and HC emissions between the simulation and the experiment at different loads, as shown in Figure 5, revealed errors within 5%. Therefore, the CFD model can be effectively used to predict marine dual-fuel engines.

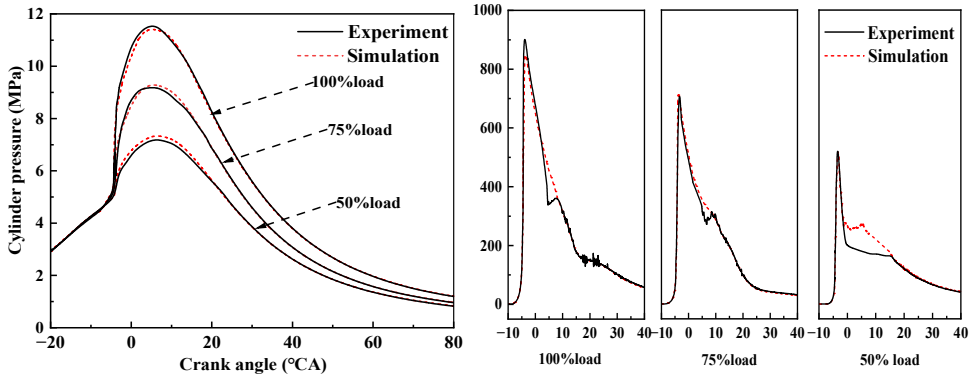

Figure 4. The HRR and cylinder pressure results.

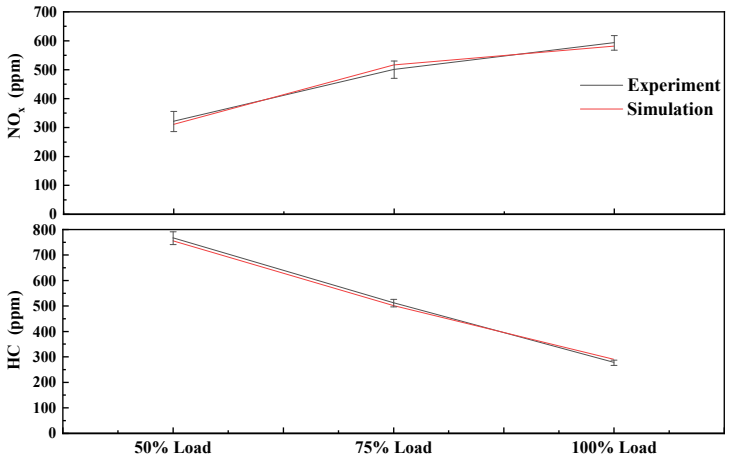

Figure 5. The emission result comparisons.

3. Effect of Biodiesel with Different Blending Ratios on Engines

Utilizing simulation theory and engine parameters from the preceding section, we incorporated a more advanced chemical reaction mechanism. This study analyzed the combustion processes of four different blends of diesel fuel: pure diesel (D100), blended fuel with 5% biodiesel (B5), blended fuel with 10% biodiesel (B10), and blended fuel with 15% biodiesel (B15), within the engine cylinder. Simulation calculations were conducted to analyze the engine's combustion, power, and emission characteristics. This included cylinder combustion pressure, temperature, and so on [37].

3.1. Characteristics of Combustion

3.1.1. In-Cylinder Pressure

Figure 6 illustrates the influence of varying biodiesel ratios on combustion cylinder pressure in cases of blended fuels. At three loads, the combustion pressure of the cylinder increased as the proportion of biodiesel in the fuel mixture increased. As an example, when the engine operated at 100% load-burning pure diesel (D100), the maximum combustion pressure reached 9.7 MPa in the cylinder. The combustion pressure in the engine cylinder reached peaks of 11.31 MPa, 11.84 MPa, and 12.40 MPa when the blended percentage was 5%, 10%, and 15%, respectively. The increased combustion pressure in the cylinder was due to the favorable oxygen content of the biodiesel, which promoted the combustion of the fuel and increased the rate of the combustion reaction [38].

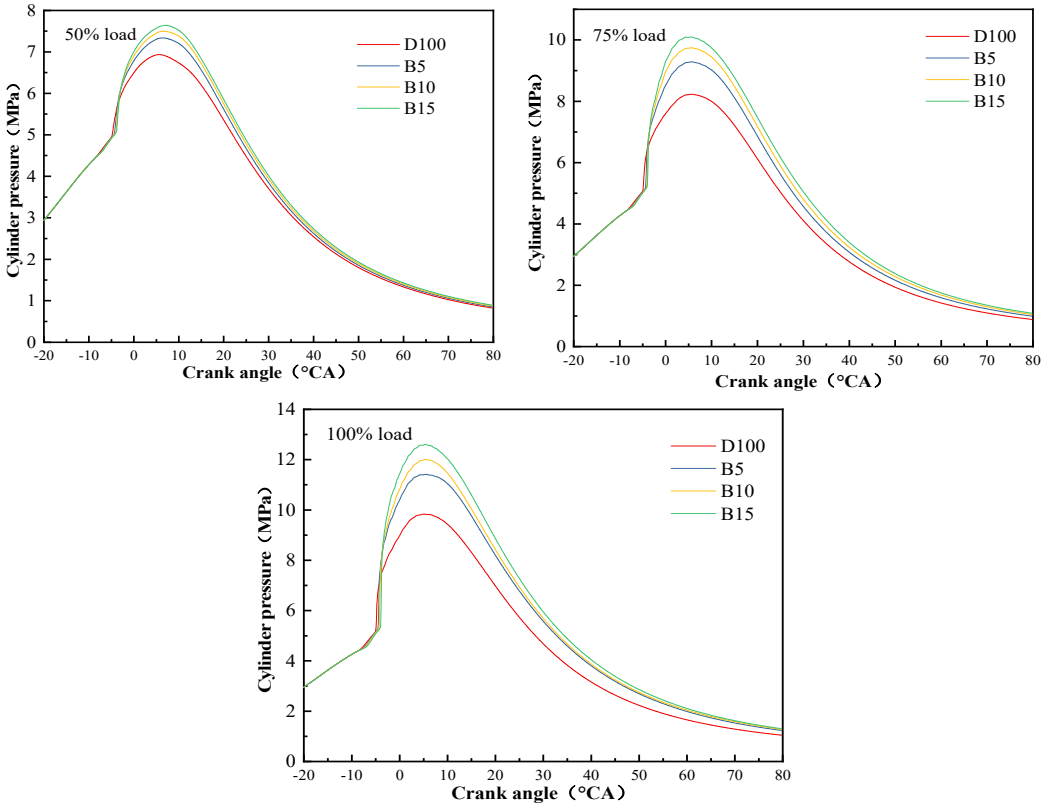

Figure 6. The impact of pressure.

3.1.2. In-Cylinder Temperature

Figure 7 illustrates how blending various percentages of biodiesel with diesel fuel affected combustion temperature within the engine cylinder, where the temperature field distribution at 100% load is shown on the right. The in-cylinder combustion temperature showed an increasing trend with increasing engine load. The substitution of diesel fuel with biodiesel led to an increase in in-cylinder combustion temperature at three different

loads. The increase in cylinder combustion temperature became more significant as the biodiesel addition rate increased.

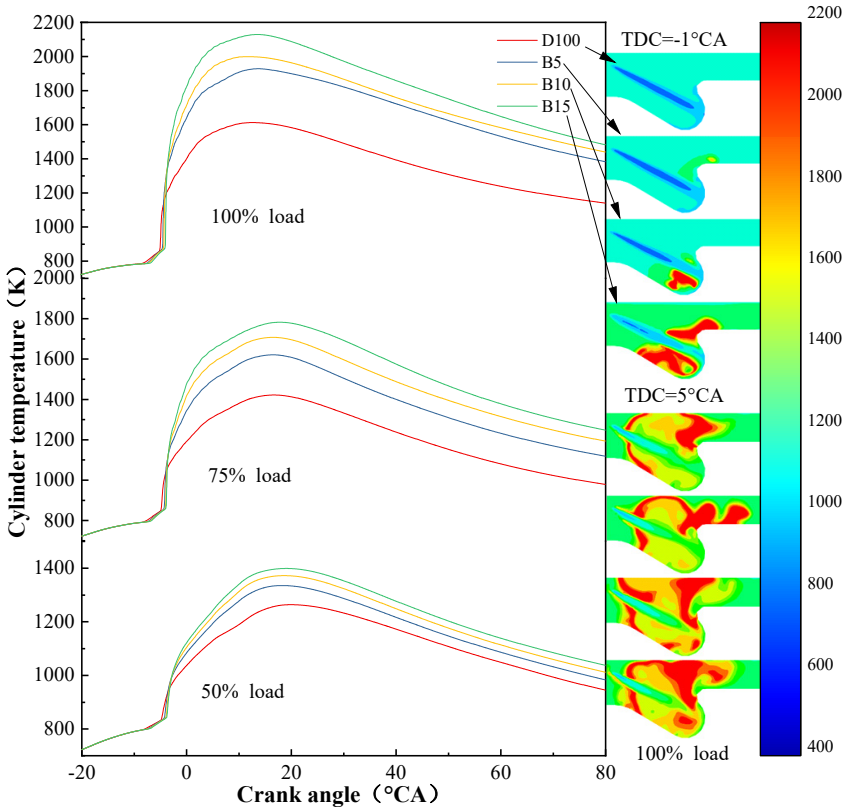

Figure 7. Combustion temperature and temperature distribution at 100% load.

For instance, when the engine burned B15 at 75% load, the in-cylinder combustion temperature was at its highest, reaching 1781.69 K. In comparison, B10, B5, and D100 result in lower temperatures of 1707.15 K, 1620.78 K, and 1421.4 K, respectively. Compared to D100, the in-cylinder combustion temperatures of the engine increased by 14.03%, 20.1%, and 25.35% when firing B5, B10, and B15, respectively. The high oxygen content of biodiesel is the main reason for its combustion-promoting properties when blended with regular diesel. The temperature field distribution shows that the local high temperature zone in the engine cylinder increased with increasing biodiesel addition. This indicates that blending biodiesel into diesel fuel can improve the combustion process and increase the temperature.

3.2. Dynamic Characteristics

3.2.1. Fuel Consumption

Figure 8 shows the effects of biodiesel addition on engine fuel consumption. As the engine load increased, the fuel consumption decreased. Under three loads, with an increase in biodiesel addition, the fuel consumption also showed an upward trend. For instance, when the engine burned D100 at 50% load, the fuel consumption was the lowest, reaching 370.27 g/(kW·h). When biodiesel additions increased to 5%, 10%, and 15%, the engine's fuel consumption also rose to 376.05, 379.74, and 382.89 g/(kW·h), respectively. The increase can be attributed to the reduction in the total calorific value of the blended fuel due to the inclusion of biodiesel, consequently resulting in higher fuel consumption.

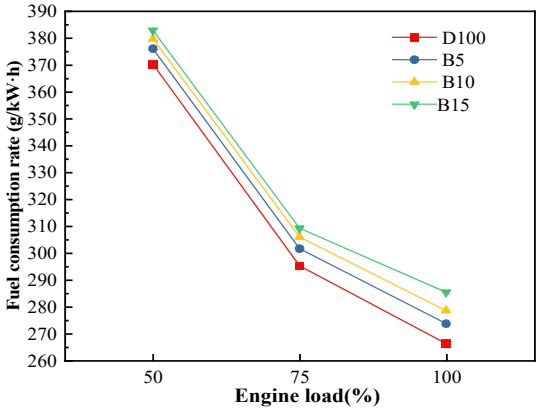

Figure 8. Fuel consumption.

3.2.2. Thermal Efficiency

Brake thermal efficiency is the ratio of the energy generated when the fuel is burned in the engine converted into useful work. The BTE can be calculated by the following Equation:

$$BTE = \frac{3600}{BSFC \cdot LCV} \tag{17}$$

where LCV is the fuel lower calorific value, MJ·kg^{-1}.

The effect of blending different percentages of biodiesel into diesel on the thermal efficiency of the engine is shown in Figure 9. This shows that as the load increased, the thermal efficiency increased [39]. In addition, the thermal efficiency of the engine continued to decrease with increasing biodiesel additions at all three loads. For instance, at 75% load, the engine exhibited the highest thermal efficiency when utilizing D100 fuel, followed by B5, B10, and B15. The thermal efficiency of the engine was reduced by 4.80%, 14.84%, and 23.10% compared to the D100 when burning the B5, B10, and B15 fuels, respectively. The thermal efficiency of the engine decreased with increasing biodiesel addition. Although the combustion was improved, the addition of biodiesel reduced the calorific value of the fuel blend and increased the viscosity of the fuel blend. Consequently, the atomization of the fuel was deteriorated, resulting in incomplete combustion of the fuel. As a result, the overall thermal efficiency decreased.

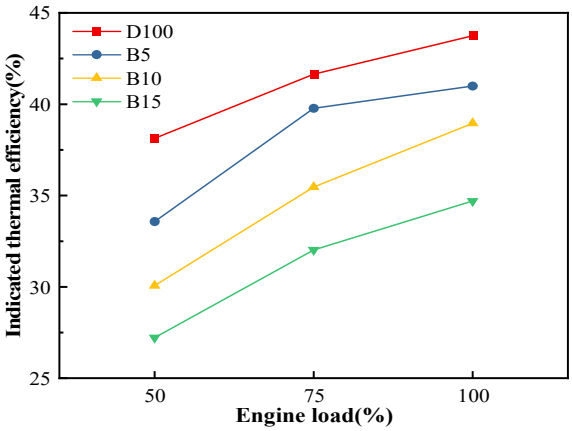

Figure 9. Effect of different biodiesel additions on thermal efficiency.

3.3. Emission Characteristic

3.3.1. Soot Emission

Figure 10 shows the effect of biodiesel addition on soot emissions from engine combustion. The figure illustrates that soot emissions showed an elevated trend as the engine load increased. This was due to the fact that as the engine load increased, the fuel supply

increased, and the in-cylinder combustion temperature rose, which promoted fuel cracking and led to higher soot emissions. At all three loads, there was a continuous decrease in soot emissions with an increasing biodiesel substitution rate. Moreover, the higher the biodiesel substitution rate, the more notable the reduction in soot emissions. Specifically, at 75% load, the engine exhibited the highest soot emissions when firing D100, followed by B5, B10, and B15. The reduction in soot emissions was mainly due to the fact that biodiesel was added, which reduced the amount of diesel fuel injected into the cycle and resulted in fewer carbon-containing fuels being burned in each cycle. Furthermore, biodiesel possesses a higher oxygen content compared to diesel. This increase in biodiesel content facilitated faster combustion, enhancing the combustion processes, and consequently contributing to lower soot emissions.

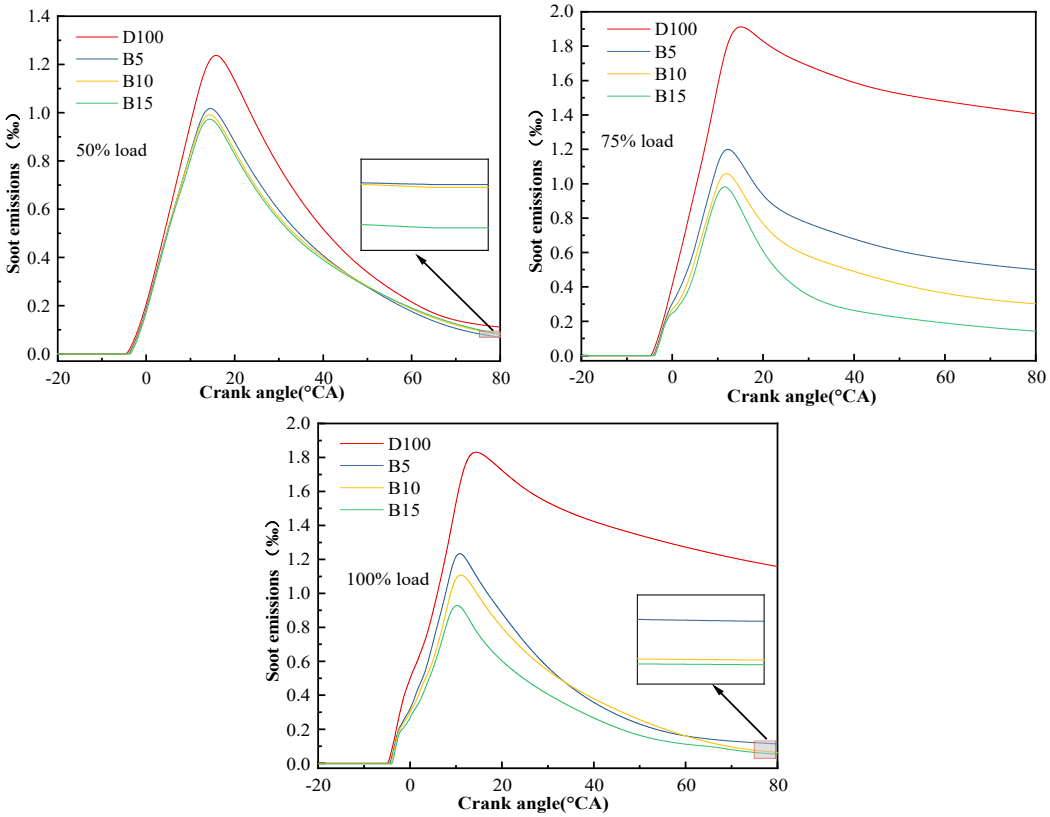

Figure 10. Effect of different biodiesel additions on soot emissions.

3.3.2. NO_x Emission

Figure 11 illustrates the impact of biodiesel addition on NO_x emissions. It is evident from the figure that as the engine load rose, NO_x emissions exhibited a continuous increase. This was due to the fact that as the engine load increased, the in-cylinder combustion temperature and combustion pressure rose, and the increase in cyclic injection also reduced the excess air coefficient, which made the high-temperature reaction time longer and promoted the generation of NO_x in the cylinder. For instance, when operating at 75% load, the engine emitted 550.11 ppm of NO_x while using D100 fuel. This figure rose to 1093.00 ppm, 1394.20 ppm, and 1590.57 ppm when using B5, B10, and B15 fuels, respectively.

The distribution of NO_x in the cylinder at 50% load is shown in the cloud diagram on the right side of Figure 11. It is evident that the in-cylinder NO_x distribution increased with higher biodiesel additions. The main reason for this is that the inclusion of biodiesel raised the oxygen content of the fuel blend, leading to an improved combustion rate and higher combustion temperatures in the cylinder [37]. Higher combustion temperatures promoted NO_x production, resulting in higher NO_x emissions in the exhaust gas [40].

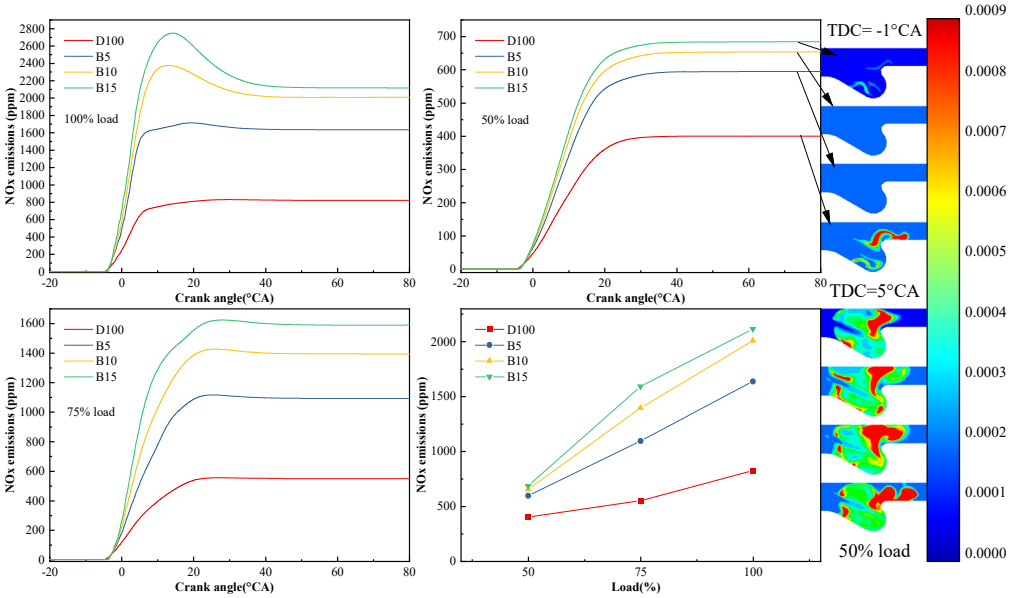

Figure 11. NO_X emissions and NO_X Distribution.

3.3.3. CO Emission

Figure 12 illustrates the impact of biodiesel addition on engine CO emissions. Across the three loads examined, the inclusion of biodiesel led to a reduction in CO emissions. For instance, at 75% load, the engine firing D100 exhibited the highest CO emission of 15,305.47 ppm, whereas CO emissions decreased to 7585.35 ppm, 4282.12 ppm, and 752.23 ppm for B5, B10, and B15, respectively. This reduction can be attributed primarily to the decreased proportion of carbon in the fuel mixture resulting from biodiesel addition. Consequently, fewer carbon-containing fuels participated in combustion, leading to decreased CO emissions. The addition of biodiesel resulted in a reduction in CO emissions, with the extent of the reduction being directly proportional to the amount of biodiesel added. This is mainly because the addition of biodiesel reduced the proportion of carbon in the fuel mixture, and less carbon-containing fuels were involved in the combustion to reduce CO emissions. The injection of biodiesel increased the oxygen concentration in the fuel mixture, accelerating combustion speed and improving fuel combustion in the cylinder. The resulting increase in combustion temperature promoted the oxidation of CO, leading to a reduction in CO emissions.

3.3.4. HC Emission

Incomplete combustion of fuel leads to HC emissions, and the addition of biodiesel had an effect on HC emissions in the tailpipe. Figure 13 shows the effect of biodiesel additions on HC emissions from the engine, and it can be seen that HC emissions were increasing as the engine load increased. This was due to the increase in load, which increased the amount of cyclic injection, resulting in there being a larger amount of over-concentrated mixture in the cylinder. The reduced oxygen concentration within the cylinder resulted in incomplete combustion and hindered the oxidation of HC emissions, thereby leading to an increase in HC emissions. Additionally, HC emissions from the engine decreased consistently across all three loads with increasing biodiesel additions. At 50% load, where the fuel injection was lower and the excess air coefficient was higher, HC emissions were naturally reduced. At 75% and 100% load, the engine released higher fuel injections, resulting in incomplete combustion of fuel. The increased involvement of fuel in diffusion combustion resulted in uneven mixing of fuel and air, consequently leading to higher HC emissions. However, the addition of biodiesel, with its higher oxygen content, promoted in-cylinder fuel combustion and thereby reduced HC emissions.

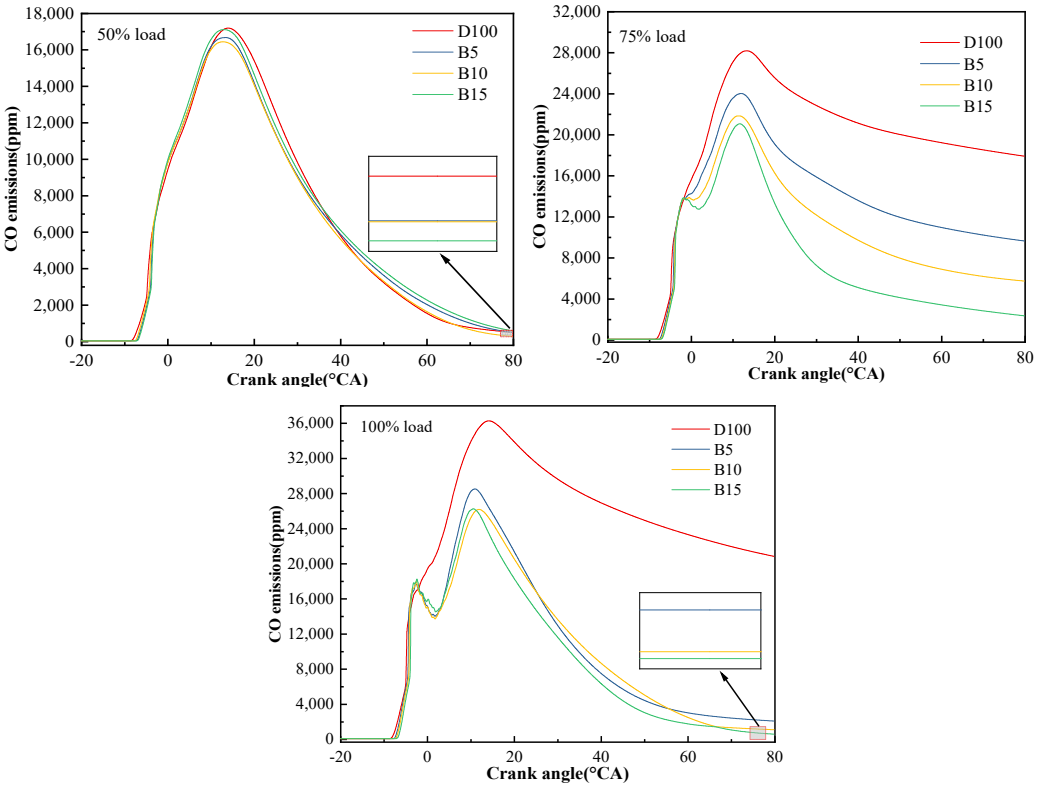

Figure 12. Effect of different biodiesel additions on CO emissions.

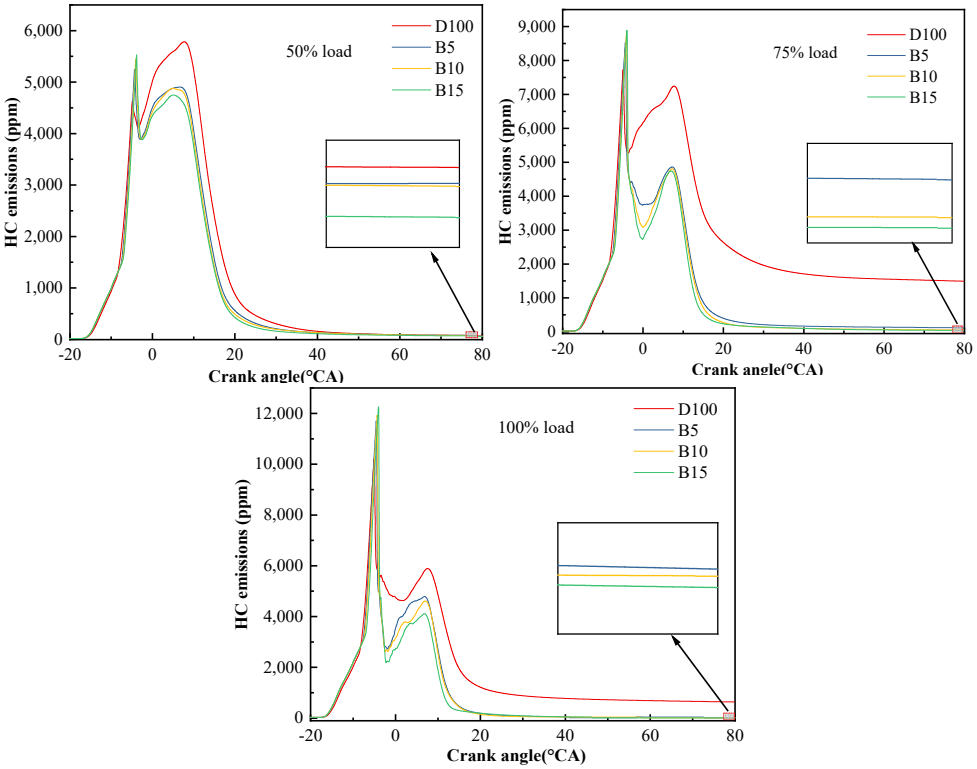

Figure 13. Effect of different biodiesel additions on HC emissions.

4. EGR Ratios

This section investigates the impact of different loads on engine combustion and emission characteristics when employing B10 blended fuel in internal combustion engines

while varying EGR rates (0%, 5%, 10%, and 15%) [41]. The impact of EGR rates on engine combustion and performance characteristics were primarily evaluated through parameters such as in-cylinder pressure, in-cylinder temperature, fuel consumption, and thermal efficiency. This study investigated the impact of various EGR rates on the emission of pollutants, including soot, NO_x, CO, and HC in engine exhaust gases.

4.1. Characteristics of Combustion

4.1.1. In-Cylinder Pressure

As the percentage of EGR increased, the ignition process was delayed due to the lower oxygen concentration and lower overall gas temperature. This delay was also reflected in the cylinder pressure curve. Figure 14 illustrates the impact of different EGR rates on in-cylinder combustion pressure under 50%, 75%, and 100% loads. The figure shows that the in-cylinder combustion pressure decreased as EGR rates increased, with a more pronounced reduction in peak in-cylinder combustion pressure at higher EGR rates. For example, at 75% load, the peak in-cylinder combustion pressure decreased by 2.85% with 5% EGR, 5.79% with 10% EGR, and 12.29% with 15% EGR, compared to no EGR. The decrease in oxygen concentration entering the cylinder due to the increase in EGR rate was the main reason for the reduced combustion rate and extended ignition delay time [32]. Furthermore, the introduction of inert gases by EGR also contributed to a certain degree of retardation in the chemical reaction rate of in-cylinder fuel combustion, resulting in a decrease in peak in-cylinder combustion pressure [42]. In addition, the noble gases increased the specific heat capacity of the intake air, which further promoted the reduction in peak in-cylinder combustion pressure.

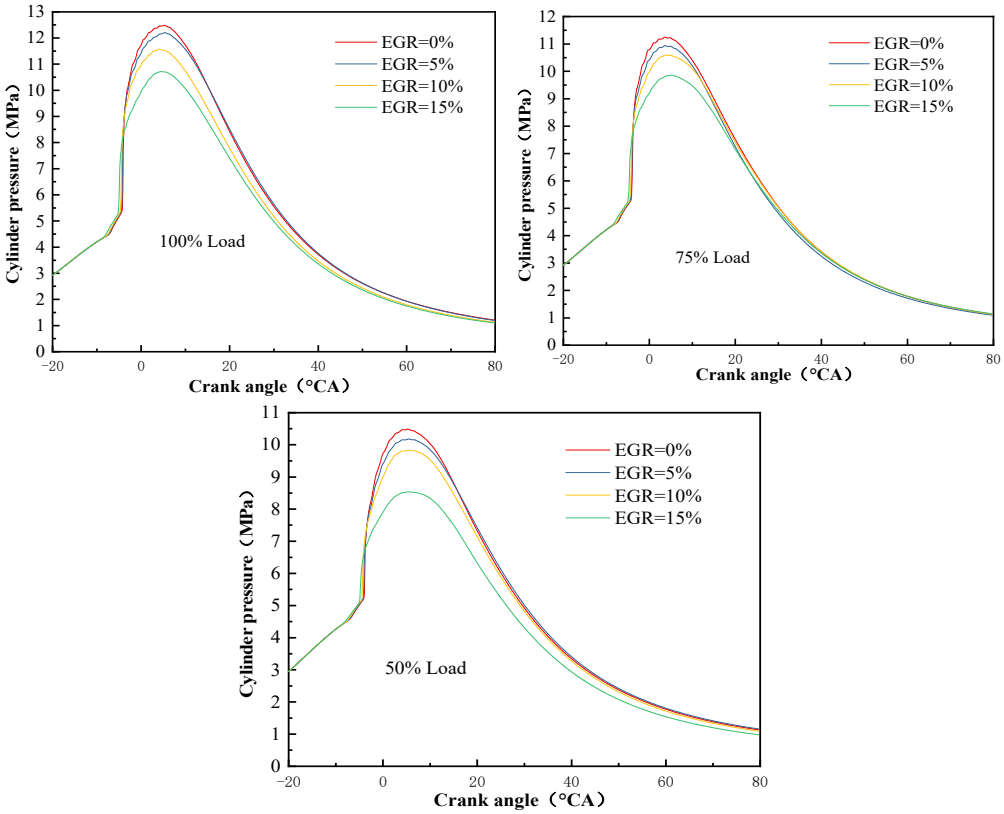

Figure 14. Effect of EGR rate on in-cylinder combustion pressure.

4.1.2. In-Cylinder Temperature

Figure 15 shows the effect of varying EGR rates on the in-cylinder combustion temperature of the engine at different loads. It is evident that the peak in-cylinder combustion temperature of the engine decreased steadily with increasing EGR rates at all loads. Further-

more, the decrease in peak in-cylinder combustion temperature became more significant with higher EGR rates. At 75% load, the highest peak in-cylinder combustion temperature occurred when EGR was not utilized. The peak temperature decreased by 2.30%, 3.49%, and 9.49% respectively when EGR rates of 5%, 10%, and 15% were employed, compared to no EGR. The decrease in in-cylinder combustion temperature was primarily attributed to the increase in inert gases in the cylinder resulting from the rise in EGR rate. The dilution of the mixture caused by this phenomenon resulted in a reduction in the combustion rate. Moreover, a rise in the EGR rate precipitated a decline in the oxygen concentration within the cylinder. The decline in the combustion temperature within the cylinder, as induced by this reduction, adversely impacted the combustion process of fuel, leading to a persistent decrease in the peak in-cylinder combustion temperature of the engine with escalating EGR rates.

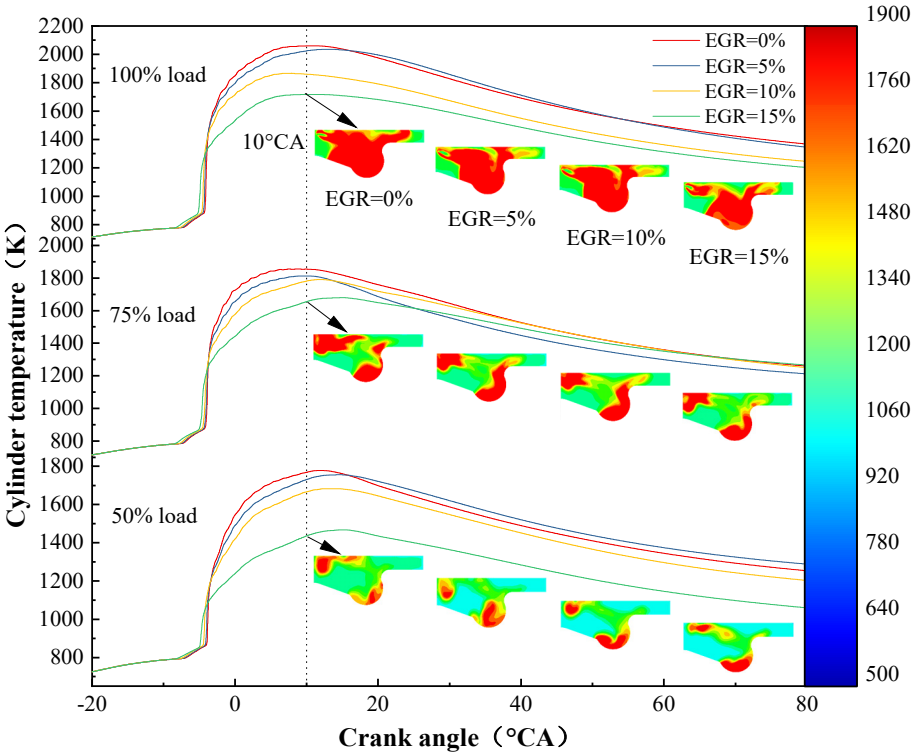

Figure 15. Combustion temperature and temperature distribution at 10 °CA.

The in-cylinder temperature distribution for an engine with a crank angle of 10 °CA at different loads and EGR rates is shown in Figure 15. At all loads, the localized high-temperature regions in the engine cylinder decreased with a continuous increase in EGR rates. This was mainly due to the decrease in oxygen concentration in the engine cylinder when higher EGR rates were employed, coupled with an increase in the specific heat capacity of intake air, both of which were unfavorable for fuel combustion inside the cylinder, resulting in a reduction in cylinder temperature.

4.2. Dynamic Characteristics

4.2.1. Thermal Efficiency

Figure 16 shows how changing the EGR rates affects how well the engine works when it is performing different amounts of work. The graph shows that as the amount of EGR goes up, the efficiency of the engine goes down, no matter how hard it is working. For instance, when the engine was working at its hardest, the efficiency went down by 2. 19%, 334%, and 449% as the EGR rate went up to 5%, 10%, and 15%, compared to not using EGR at all. This decrease in engine thermal efficiency can be attributed to the increase in exhaust gas content in the engine cylinder with higher EGR rates. This exerted a certain

inhibitory effect on the combustion process of in-cylinder fuel. Therefore, it is important to maintain a balance between EGR rates and engine thermal efficiency. Additionally, the increase in exhaust gas content in the intake air led to a decrease in oxygen concentration in the cylinder, creating a state of oxygen deficiency inside the cylinder. This state was unfavorable for the complete combustion of fuel [43].

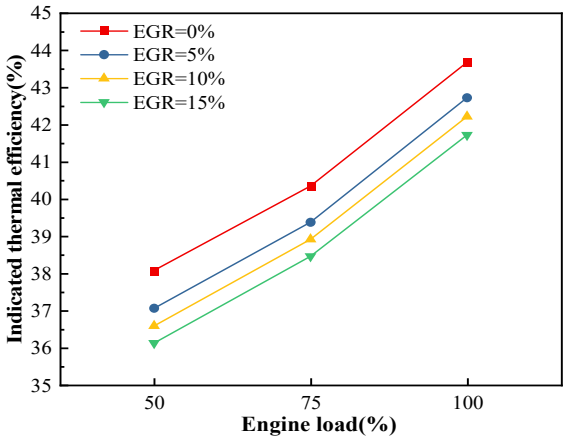

Figure 16. Effect of EGR rate on thermal efficiency.

4.2.2. Fuel Consumption

Figure 17 illustrates the effects of different EGR rates on engine fuel consumption at various loads. The figure indicates that engine fuel consumption increased steadily with increasing EGR rates at all loads. For example, when operating at 50% load, the engine's fuel consumption without EGR was 370.72 g/(kW·h). At a 5% EGR rate, fuel consumption rose to 376.23 g/(kW·h). Increasing the EGR rate to 10% resulted in a further rise to 378.97 g/(kW·h), while at 15%, it climbed to 381.87 g/(kW·h). These increments corresponded to 1.49%, 2.23%, and 3.01%, respectively. The increase in the EGR rate was primarily responsible for this phenomenon. This led to a higher quantity of exhaust gases entering the cylinder, which in turn reduced the oxygen concentration inside the cylinder. This created localized oxygen-deficient zones and inhibited the chemical reaction process of in-cylinder fuel combustion. As a result, incomplete combustion of fuel occurred, leading to a continuous increase in engine fuel consumption [44].

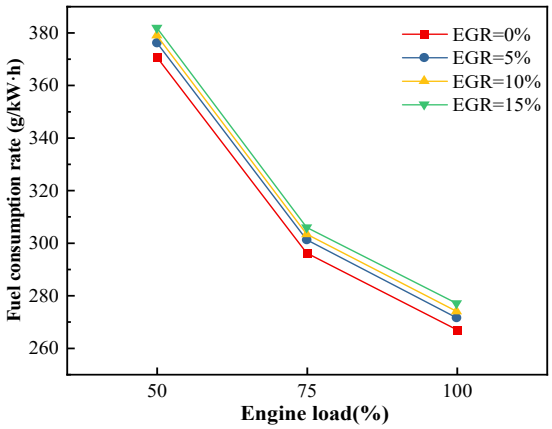

Figure 17. Fuel consumption rate.

4.3. Emission Characteristic

4.3.1. Soot Emission

Figure 18 depicts how different EGR rates affected soot emissions from the engine under various load conditions. The figure shows that soot emissions increased initially and then decreased with crank angle across the three loads. This was due to the continuous

oxidation of early-formed soot during the combustion process, leading to a reduction in soot emissions in the later stages of combustion. Furthermore, as the engine EGR rate increased, soot emissions also increased continuously. The primary reason for this phenomenon lies in the reduction in the oxygen concentration within the cylinder as the EGR rates increased. This decline notably impacted the oxidation process of soot, consequently leading to heightened soot emissions. Furthermore, an increase in the EGR rate resulted in a significant reduction in the generation rate and peak mass of OH radicals. This was due to a decrease in the in-cylinder temperature, which weakened the oxidation effect of OH radicals on soot, leading to an increase in soot emissions [45]. Additionally, higher EGR rates led to an increase in the formation of soot precursors, which further contributed to increased soot emissions. This is because the oxidation process of soot precursors was inhibited at higher EGR rates [46].

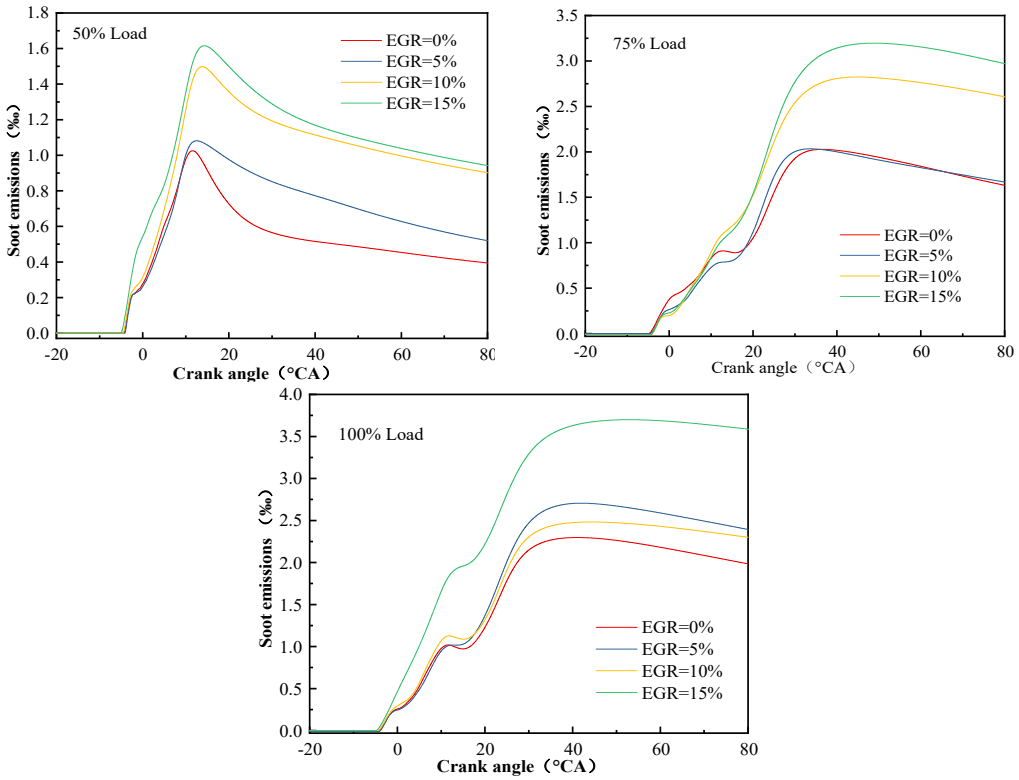

Figure 18. Effect of EGR rate on soot emissions.

4.3.2. NO_x Emission

Figure 19 demonstrates the effect of varying EGR rates on NO_x emissions from the engine across different load conditions. The graph reveals a consistent reduction in NO_x emissions as EGR rates increased across all loads. For instance, at 100% load, the NO_x emission peaked at 681.48 ppm without EGR utilization. However, with an EGR rate of 5%, this value diminished to 484.62 ppm, further dropping to 312.06 ppm with a 10% EGR rate, and reaching 174.47 ppm with a 15% EGR rate. The reduction in average cylinder temperature with EGR utilization primarily caused a decrease in in-cylinder combustion temperature, which significantly influenced NO_x emissions. The activation energy associated with NO_x formation reactions decreased as the in-cylinder combustion temperature decreased with EGR, leading to a reduction in in-cylinder NO_x emissions. With increasing EGR rates, more exhaust gas was introduced into the cylinder, which reduced the oxygen concentration involved in combustion and affected the ignition and combustion process of in-cylinder fuel. Additionally, increased EGR led to an increase in exhaust gas content in the intake air, which further increased the specific heat capacity of

the intake air, resulting in a decrease in in-cylinder temperature [47]. The reduction in NO_x emissions was a result of these factors [48].

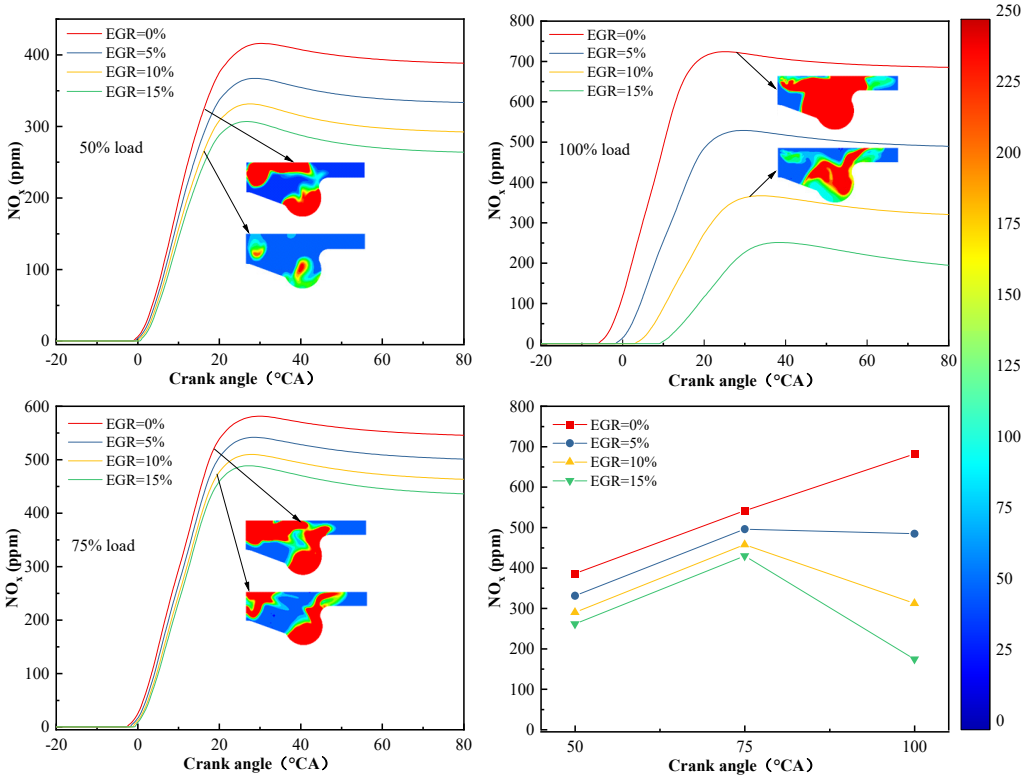

Figure 19. NO_x emissions and distribution.

Figure 19 illustrates the contour map of the in-cylinder NO_x distribution of the engine under different loads and EGR rates. It can be observed that the in-cylinder NO_x distribution decreased with the continuous increase in EGR rates at all loads. Furthermore, when juxtaposed with the contour map depicting the distribution of in-cylinder combustion temperatures, as illustrated in Figure 15, it becomes evident that NO_x primarily accumulated in areas characterized by elevated temperatures. Temperature is a crucial factor that affects the generation of NO_x emissions. Increasing the EGR rates led to a decrease in in-cylinder combustion temperature, which was unfavorable for NO_x pollutant generation, resulting in reduced NO_x emissions.

4.3.3. CO Emissions

Figure 20 illustrates the impact of different exhaust gas recirculation (EGR) rates on CO emissions from the engine under various loads. The figure shows that CO emissions initially increased and then decreased with the increase in crank angle. This was due to the oxidation of early-formed CO pollutants during combustion, leading to a decrease in CO emissions. CO emissions increased continuously with increasing EGR rates at all loads. Higher EGR rates resulted in a more pronounced increase in CO emissions. This is because the production of CO was mainly influenced by temperature and oxygen content [49]. When EGR was not utilized, the relatively higher temperature and oxygen content inside the cylinder had a smaller impact on CO emissions compared to the scenario with EGR. As EGR rates increased, exhaust gas was introduced into the cylinder, reducing oxygen concentration and promoting the formation of oxygen-deficient regions. This led to increased CO emissions. Furthermore, EGR utilization increased the exhaust gas content in the intake air, thereby raising the specific heat capacity of the mixture and lowering the combustion temperature inside the cylinder. The lower temperature and oxygen content were unfavorable for CO oxidation, resulting in increased CO emissions [50].

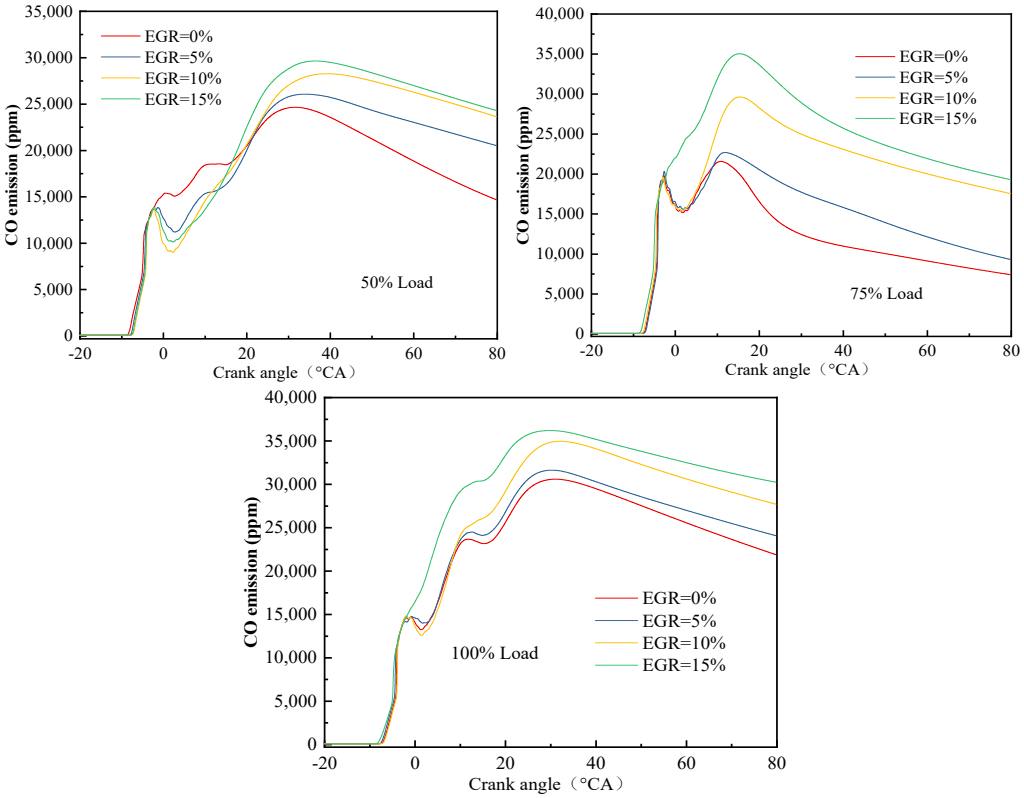

Figure 20. Effect of EGR rate on CO emissions.

4.3.4. HC Emission

Figure 21 showcases how different EGR rates influenced HC emissions from the engine across various load conditions. The graph illustrates a consistent rise in HC emissions as EGR rates increased at all loads. This trend stemmed from the reduction in oxygen content within the cylinder due to increased EGR rates, consequently diminishing the engine's combustion efficiency. As a result, the flame was more likely to extinguish near the cylinder wall during combustion, leading to incomplete fuel combustion and increased HC emissions [51], which are one of the primary sources of HC emissions. Moreover, the escalation of EGR rates led to a decrease in both in-cylinder combustion temperature and oxygen content. This alteration significantly impacted the oxidation process of HC, ultimately culminating in an upsurge in HC emissions.

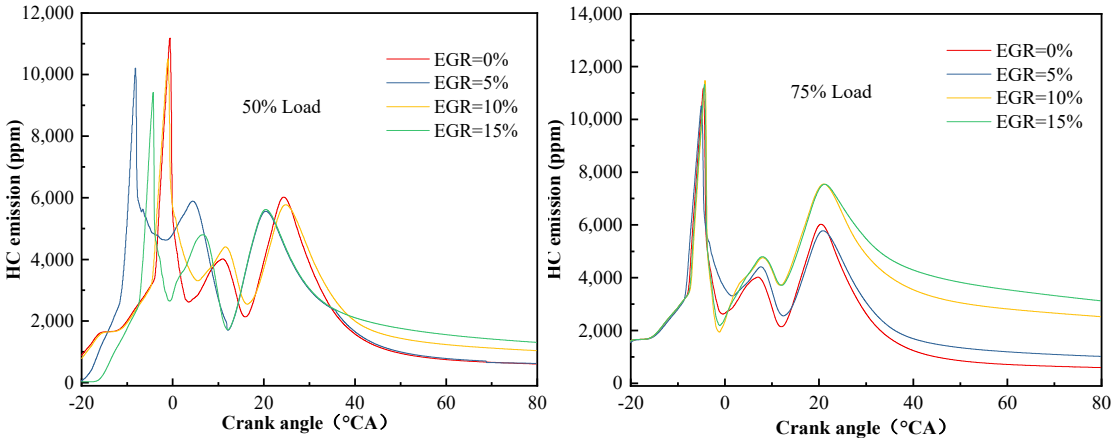

Figure 21. *Cont.*

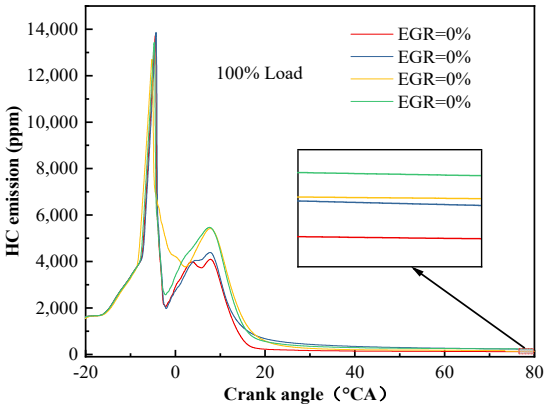

Figure 21. Effect of EGR rate on HC emissions.

5. Multi-Objective Optimization Based on Response Surface Methodology

This study focused on the optimization of combustion and emission characteristics of a dual-fuel engine based on three factors: load, blend ratio of canola oil, and EGR. Response surface methodology was employed to conduct multi-objective optimization of the dual-fuel engine [52]. The primary objective was to enhance the BTE of the diesel engine while reducing BSFC, as well as the emissions of nitrogen NO_x, HC, and CO under high engine loads by incorporating canola oil and EGR. The ultimate objective was to ascertain the most advantageous operational parameters for the dual-fuel engine utilizing biodiesel.

5.1. Model Fitting Analysis and Evaluation

In the present study, response surface methodology was used to establish a response surface model for dual-fuel engines to predict their combustion and emission performance. Based on the above research scope, the Box–Behnken experimental design method was used to design experiments for the following parameters: engine load from 50% to 100%, canola oil addition rate from 0% to 15%, and EGR rate from 0% to 15%. Initially, it is essential to incorporate the pertinent input variables into the mathematical model of the response surface.

5.2. Analysis and Evaluation of Fitting Model

Utilizing the least squares method, the response variables, including BSFC, BTE, HC, and NO_x emissions, were fitted based on the simulated results obtained through design. The regression equations for each response variable in the response surface model are presented below:

$$BSFC = 327.02 - 41.69x - 47.48y + 22.78z - 0.6412xy - 8.81xz + 5.1\mathrm{yz} - 5.8\mathrm{x}^2 + 5.2y^2 + 15.49z^2 \quad (18)$$

$$BTE = 38.48 + 1.66x + 2.28y - 0.8256z + 0.9258xy - 0.0036xz - 0.3501yz - 0.3566x^2 + 0.5551y^2 + 0.2567z^2 \quad (19)$$

$$HC = 563.16 - 115.55x - 237.61y + 32z - 12.47xy + 35.56xz + 29.81yz - 45.88x^2 + 2.06y^2 - 25.63z^2 \quad (20)$$

$$NOx = 400 + 138.35x + 119.17y - 72.01z + 45.9xy - 13.29xz - 24.23yz + 17.97x^2 - 10.86y^2 + 15.40z^2 \quad (21)$$

where x, y, and z denote the canola oil addition fraction, load fraction, and EGR, respectively.

The ANOVA parameters are shown in Tables 4 and 5. From the tables, it can be seen that the p-values of the quadratic model were all less than 0.0001. Therefore, the response surface model showed good predictability and agreement with experimental results.

Table 4. Analysis of variance table of BSFC and BTE.

Parameter	BSFC		BTE	
	F-Value	***p*-Value**	**F-Value**	***p*-Value**
Model	162.68	<0.0001	144.65	<0.0001
x	459.82	<0.0001	412.71	<0.0001
y	630.04	<0.0001	789.65	<0.0001
z	161.20	<0.0001	120.23	<0.0001
xy	0.0687	0.7897	79.01	<0.0001
xz	12.98	0.0048	0.0013	0.9697
yx	4.56	0.0653	12.02	0.0073
x^2	2.99	0.1203	6.21	0.0296
y^2	2.96	0.1173	18.34	0.0017
z^2	20.89	0.0010	3.16	0.1073
R^2	0.9928		0.9923	
Adj-R^2	0.9873		0.9854	
Pred-R^2	0.9398		0.9381	

Table 5. Analysis of variance of HC and NO_x.

Parameter	HC		NO_x	
	F-Value	***p*-Value**	**F-Value**	***p*-Value**
Model	189.68	<0.0001	536.40	<0.0001
x	284.46	<0.0001	2224.93	<0.0001
y	1252.22	<0.0001	1715.82	<0.0001
z	24.89	0.0005	689.08	<0.0001
xy	2.12	0.1812	152.72	<0.0001
xz	17.20	0.0020	13.10	0.0047
yx	11.81	0.0064	42.54	<0.0001
x^2	14.82	0.0032	12.41	0.0055
y^2	0.0364	0.8525	5.54	0.0404
z^2	4.55	0.0587	8.96	0.0135
R^2	0.9842		0.9978	
Adj-R^2	0.9789		0.9962	
Pred-R^2	0.9623		0.9651	

The difference between the predicted values and the actual values is called the residual. Figure 22a–d present a numerical comparison of the actual and predicted levels for the engine. The figures depict that the deviations between the predicted and experimental data for the engine fall within the ideal range. Furthermore, a proportional relationship between the predicted and actual values was evident. Demonstrating the accuracy of established models for predicting dual fuel engine performance, all regression models for the response shown in the figures had a good fit at the 95% confidence level.

5.3. Optimization Results Analysis

5.3.1. Specific Fuel Consumption for Brakes

BSFC denotes the effective power output of an engine utilizing various fuels over a defined time interval. In Table 4, it is evident that the fractions of canola oil, engine load, and EGR significantly influenced the engine ($p < 0.0001$). Furthermore, the coefficients of determination R^2, Adj-R^2, and Pred-R^2 for BSFC response values were 99.28%,98.73%, and 93.98%, respectively, demonstrating the exceptional suitability of this model for BSFC prediction.

The BSFC surface plots of separate variables at different loads are depicted in Figure 23a–c. Higher values of the F-statistic in Table 4 correspond to a greater influence on BSFC. Therefore, the sequence of factors affecting BSFC emissions was as follows: engine load > canola oil ratio > EGR. Among these, engine load exhibited a positive correlation with BSFC. This is because an increase in load improved the combustion conditions of the engine, leading to a

reduction in BSFC. However, the effect of EGR on BSFC initially changed slowly, followed by a significant increase in BSFC with an increase in EGR. Increasing the EGR rate reduced the oxygen concentration in the engine cylinder, resulting in inadequate fresh air intake and deteriorated combustion, ultimately increasing BSFC. Therefore, higher loads contributed to a reduction in BSFC.

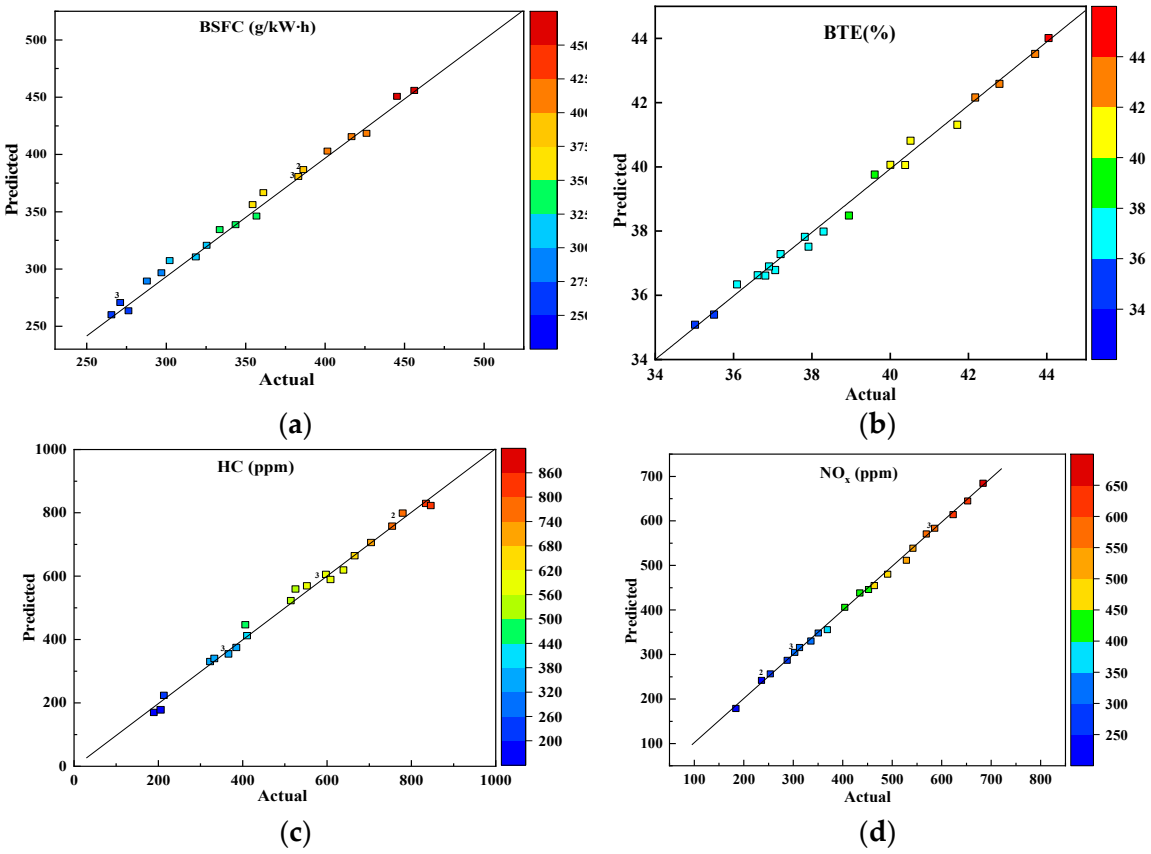

Figure 22. Forecast vs. actual mzetrics. (**a**) BSFC comparative graph; (**b**) BTE comparative graph; (**c**) HC emission comparative graph; (**d**) NO_x emission comparative graph.

5.3.2. Thermal Efficiency

Table 4 displays the impact parameters of canola oil proportion, EGR, and load on engine BTE, revealing their notable effects on BTE ($p < 0.0001$). Moreover, the noteworthy p-values of the quadratic terms signify the presence of quadratic impacts. Furthermore, the high values of R^2, Adj-R^2, and Pred-R^2, standing at 99.23%, 98.54%, and 93.81%, respectively, demonstrate the model's exceptional predictive capability for BTE.

Figure 24a–c illustrate the BTE surface plots depicting the influence of different variables across various loads. It can be observed that the order of variables influencing BTE was as follows: load > canola oil percentage > EGR. Particularly, an increase in load led to a noticeable enhancement in BTE, especially at higher loads. This was attributed to the increased intake volume as the load rose, which significantly improved combustion conditions within the engine cylinder, consequently boosting BTE. Across all scenarios, as EGR varied from 0% to 15%, BTE exhibited a decreasing trend. Elevated EGR levels diluted the concentration within the engine cylinder, diminishing the combustion reaction rate, and consequently leading to a decline in BTE. Therefore, optimal BTE can be attained at higher loads.

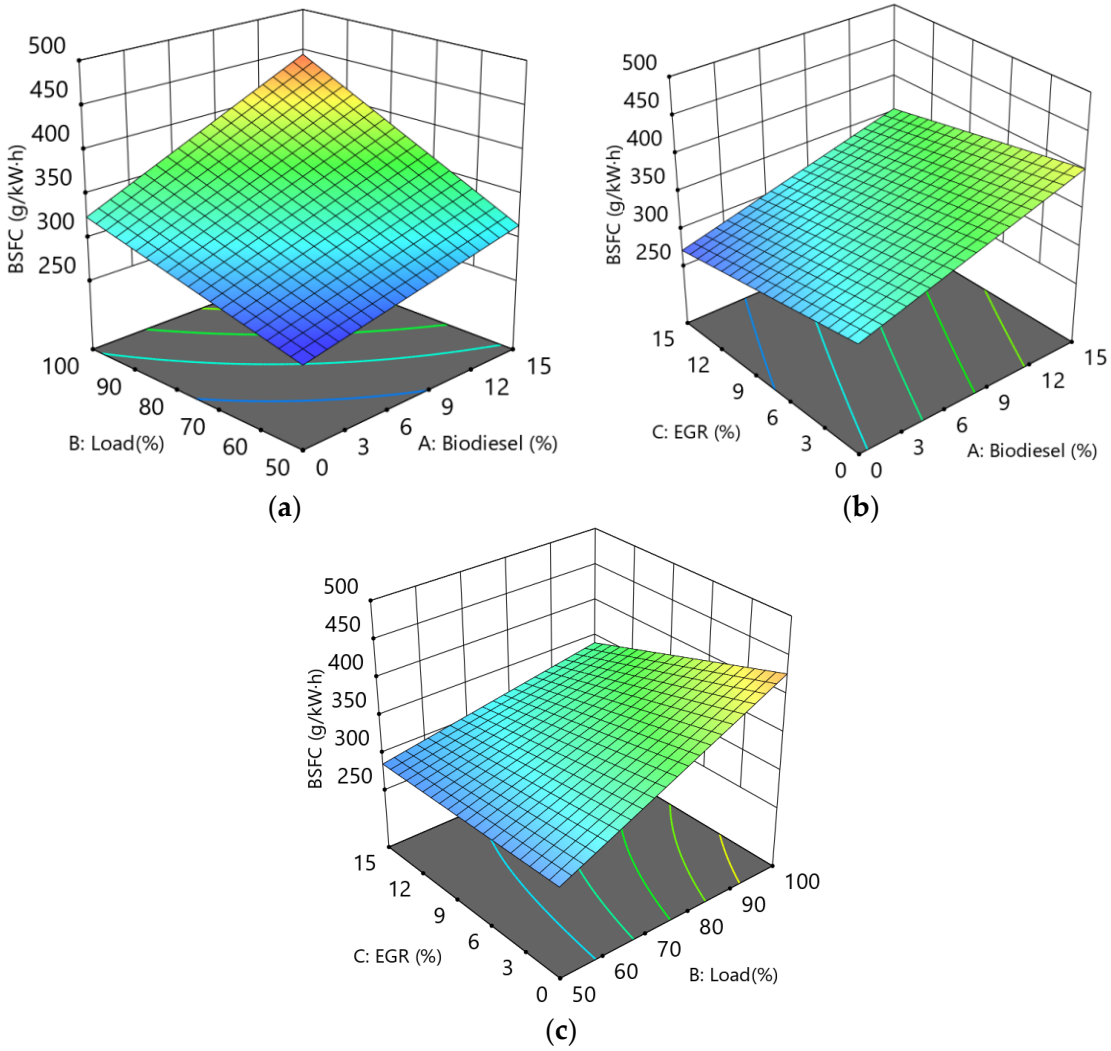

Figure 23. Surface plots of the effect of different variables on BSFC. (**a**) Different load rates and biodiesel additions on BSFC; (**b**) Different EGR rates and biodiesel additions on BSFC; (**c**) Different EGR rates and load rates on BSFC.

5.3.3. HC Emission

Table 5 displays the influence parameters of canola oil proportion, engine load, and EGR on engine HC emissions, revealing the significant impact of all three variables on HC emissions ($p < 0.0001$). Additionally, the elevated values of R^2, Adj-R^2, and Pred-R^2, standing at 98.42%, 97.89%, and 96.23%, respectively, indicate the model's outstanding predictive ability for HC emissions.

Figure 25a–c illustrate the HC surface plots showcasing the impact of different variables across various loads. The sequence of variables impacting HC emissions was evident as follows: load > canola oil percentage > EGR, with load exerting the most pronounced influence. As load escalated, HC emissions notably diminished, particularly at 100% load, where unburned HC emissions reached their nadir. This phenomenon can be ascribed to the substantial enhancement in combustion conditions within the engine cylinder with increasing load, resulting in more thorough combustion. The elevation in biodiesel content led to an augmentation in concentrations of H and OH radicals within the engine cylinder, accompanied by an increase in cylinder temperature, collectively contributing to the reduction in HC emissions. Therefore, larger loads and higher biodiesel percentages contributed to a reduction in HC emissions.

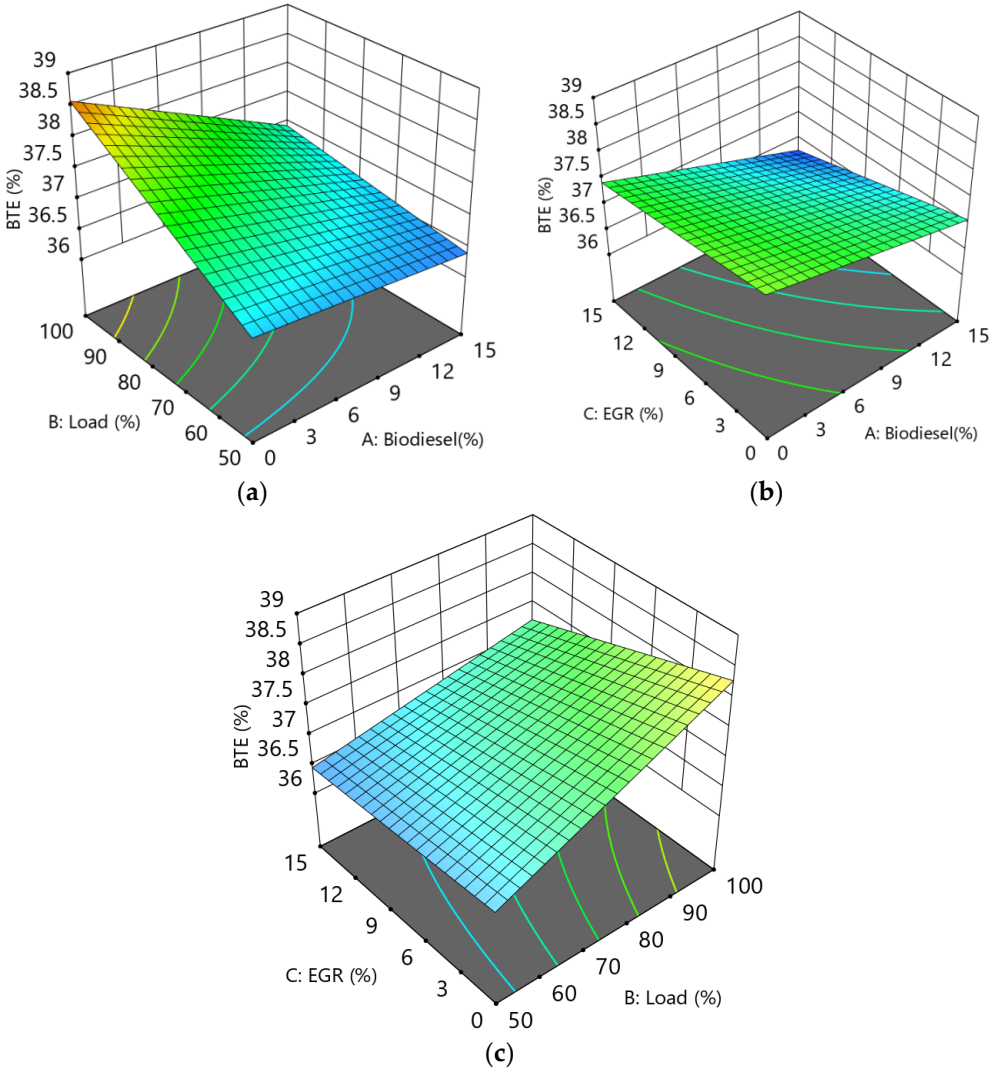

Figure 24. Surface plots of the effect of different variables on BTE. (**a**) Different load rates and biodiesel additions on BTE; (**b**) Different EGR rates and biodiesel additions on BTE; (**c**) Different EGR rates and load rates on BTE.

5.3.4. NO_x Emission

The primary factors influencing NO_x emissions included the oxygen concentration and the temperature within the engine cylinder. The impact parameters of biodiesel blends, engine load, and EGR on engine NO_x emissions are presented in Table 5, demonstrating the significant effects of these three variables on NO_x emissions ($p < 0.0001$). Furthermore, the values of R^2, Adj-R^2, and Pred-R^2 for the response of NO_x emissions stand at 99.78%, 99.62%, and 96.51%, respectively, indicating the high suitability of the model for predicting NO_x emissions.

Figure 26a–c display the surface plots depicting NO_x emissions under various conditions across different loads. It is evident that the magnitude of the effect on NO_x emissions followed the order EGR > canola oil percentage > load, with EGR having the most significant effect on NO_x emissions. This was mainly due to the decrease in fresh air and oxygen concentration that resulted from the increased EGR, which led to a reduction in flame propagation speed and a slower rise in temperature. In addition, both high biodiesel blends and high engine load increased the cylinder temperature, which promoted nitrogen–oxygen reactions and resulted in the formation of a large amount of NO_x. Hence, EGR emerged as a crucial factor in mitigating NO_x emissions. By introducing appropriate EGR under high loads and canola oil addition, optimal NO_x emissions can be achieved.

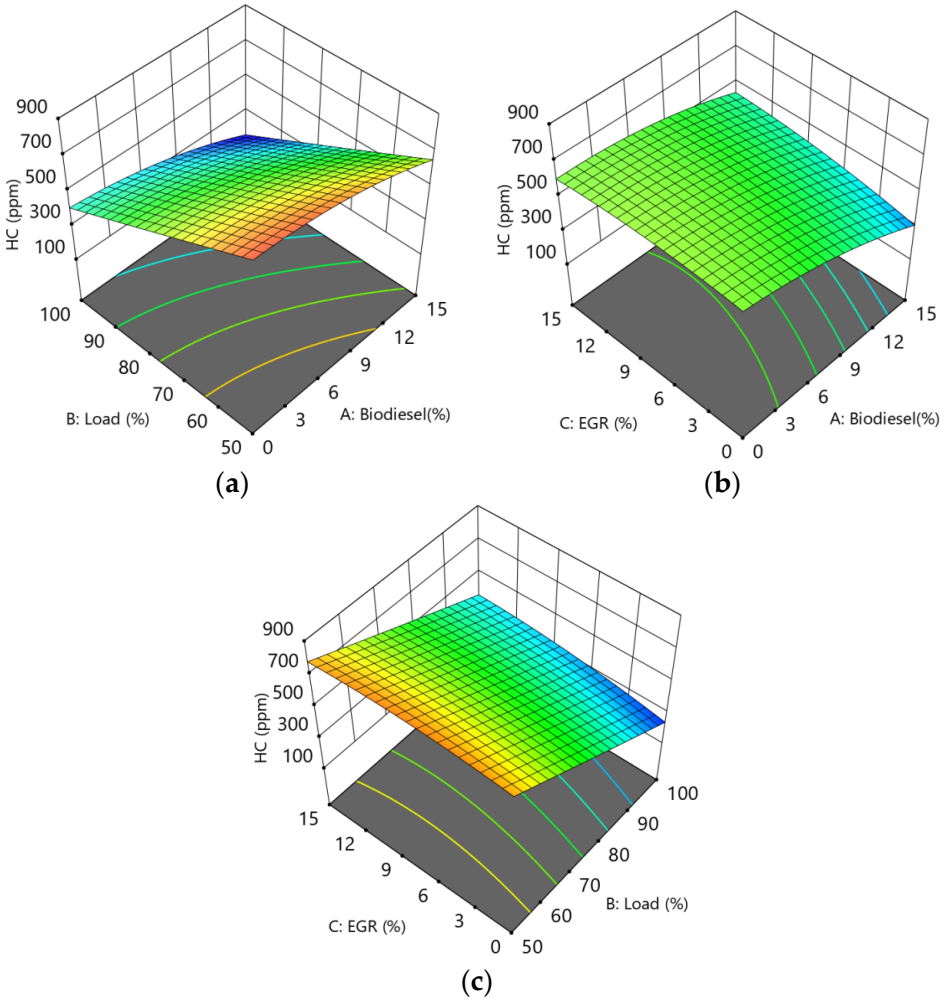

Figure 25. Surface plots of the effect of different variables on HC emission. (**a**) Different load rates and biodiesel additions on HC emission; (**b**) Different EGR rates and biodiesel additions on HC emission; (**c**) Different EGR rates and load rates on HC emission.

5.3.5. Multi-Objective Optimization

In this section, a response surface methodology was utilized to perform multi-objective optimization of the engine. The goal was to attain higher BTE while simultaneously lowering BSFC, HC, and NO_x emissions under high engine load conditions through the incorporation of both canola oil and EGR. Ultimately, the optimal solution yielded an ideal value of 0.788. Accordingly, the optimal input parameters were identified as 6.9% canola oil fraction, 100% engine load, and 7.7% EGR. Contour plots of BSFC, BTE, HC, and NO_x emissions at the maximum expected value after optimization are shown in Figure 27. Considering the optimized input parameters, the best values of BSFC, BTE, HC, and NO_x emissions were determined as 282.62 g/(kW·h), 38.15%, 410.37 ppm, and 274.38 ppm, respectively.

Overall, the three factors significantly influenced the desired output responses, statistically contributing to an enhancement in BTE and reduction in BSFC, NO_x, and HC emissions. Moreover, EGR demonstrated significant statistical significance in reducing NO_x emissions. It is noteworthy that post-multi-objective optimization using RSM, the combustion and emission characteristics of the dual-fuel engine experienced substantial improvements when appropriate amounts of canola oil and EGR were utilized.

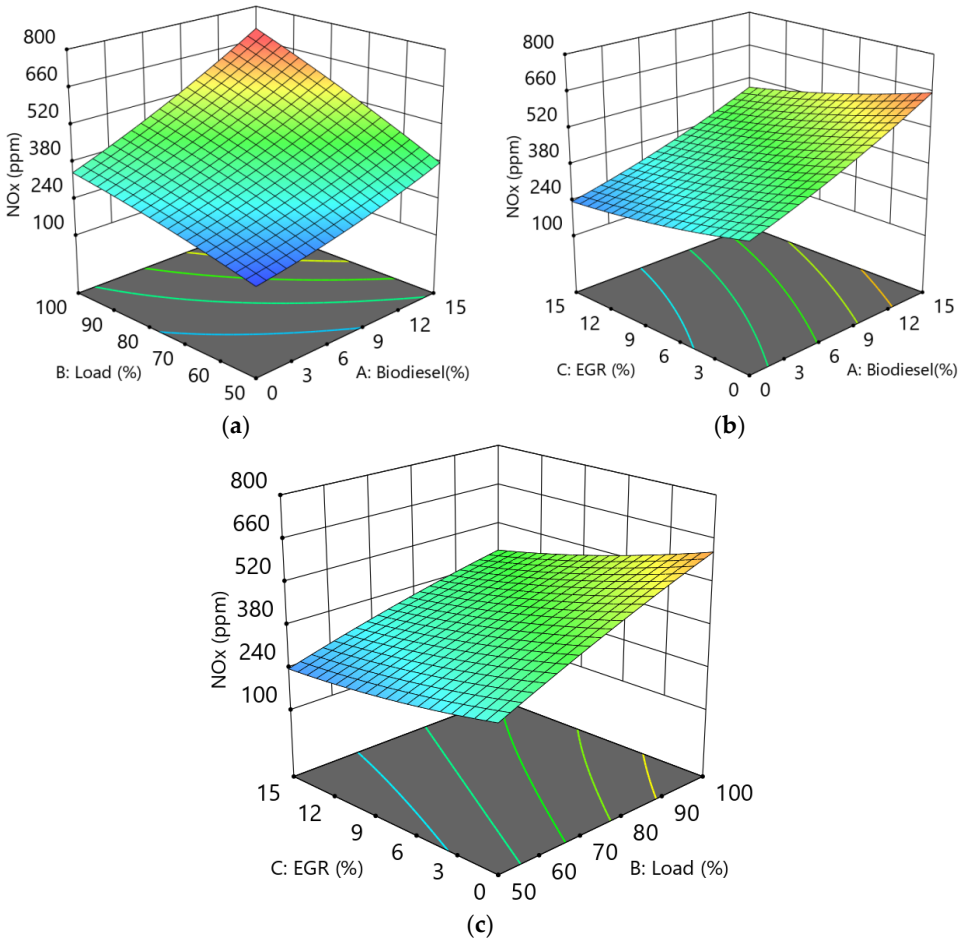

Figure 26. Surface plots of the effect of different variables on NO_x emission. (**a**) Different load rates and biodiesel additions on NO_x emission; (**b**) Different EGR rates and biodiesel additions on NO_x emission; (**c**) Different EGR rates and load rates on NO_x emission.

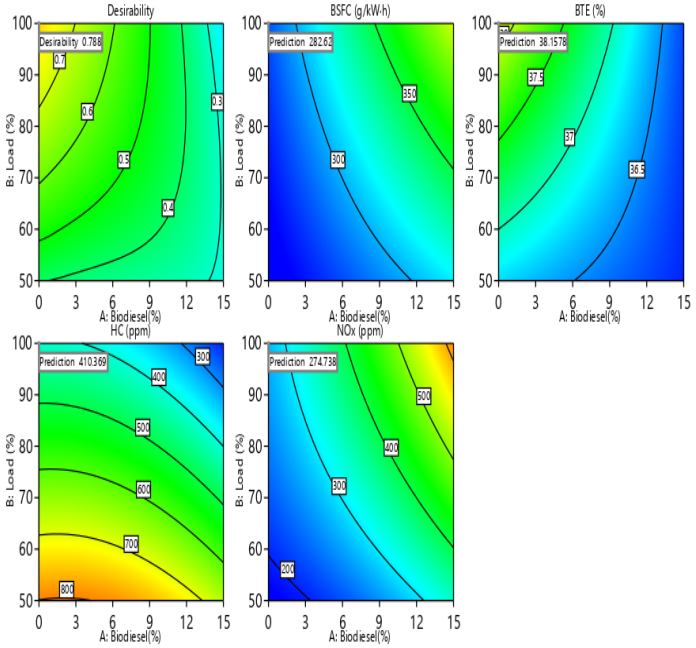

Figure 27. Load and biodiesel energy fraction contour plots for desirability, BSFC, BTE, HC, and NO_x emissions.

To validate the accuracy of the response surface optimization results, experimental tests were performed on the dual-fuel engine. Table 6 presents the experimental values, predicted values, and error ratios of the dual-fuel engine. It is evident that there exists a substantial correlation among all the output responses. The discrepancies between the experimental and predicted values for BSFC, BTE, HC, and NO_x emissions were relatively minor, standing at −0.761%, 0.370%, −1.199%, and 3.699%, respectively. Thus, the established response surface model demonstrated high prediction accuracy for the dual-fuel engine.

Table 6. Comparison of predicted and experimental results.

Biodiesel%	Load%	EGR%	Parameter	BSFC (g/kW·h)	BTE (%)	HC (ppm)	NO_x (ppm)
6.9	100	7.7	Actual	280.47	38.29	405.45	284.53
			Predicted	282.62	38.15	410.37	274.38
			Error(%)	−0.761	0.370	−1.199	3.699

6. Conclusions

This research delved into exploring the combustion and emission characteristics of a dual-fuel engine utilizing biodiesel blends, employing both simulation and experimental approaches. Initially, an accurate 3D CFD model was devised to simulate the engine's fuel injection, combustion, and emission processes. Following this, the investigation delved into assessing the influence of varying biodiesel blend ratios on key parameters such as in-cylinder pressure, combustion temperature, and BSFC, as well as emissions of NO_x, HC, and CO, leveraging the established model. Furthermore, the study scrutinized the impact of different EGR rates on the performance of the biodiesel dual-fuel engine. Ultimately, employing a multi-objective optimization approach via RSM, the research aimed to optimize BTE while concurrently minimizing BSFC, NO_x, HC, and CO emissions across different engine loads, blend ratios, and EGR rates, thus identifying the most favorable operational conditions for engine. Hereunder is the condensed overview of the entire investigation:

(1) Increasing the biodiesel proportion in the fuel blend at 50%, 75%, and 100% loads amplified the cylinder pressure and temperature. This augmentation was more conspicuous at higher biodiesel ratios. Nonetheless, integrating biodiesel affected the engine's economic viability. Irrespective of the load conditions examined, higher biodiesel ratios correlated with heightened fuel consumption and diminished thermal efficiency. Additionally, raising the biodiesel content substantially reduced soot, CO, and HC emissions in the exhaust, albeit at the expense of escalated NO_x emissions.

(2) At 50%, 75%, and 100% engine loads, elevating the EGR rate diminished both cylinder combustion temperature and pressure. This reduction was more pronounced at higher EGR rates. However, the utilization of EGR technology in the engine did affect its economic performance to a certain extent. Across all loads investigated, augmenting the EGR rate led to increased fuel consumption and decreased thermal efficiency of the engine. Furthermore, raising the engine's EGR rate markedly diminished NO_x emissions in the exhaust, albeit resulting in elevated emissions of soot, CO, and HC.

(3) Increasing the engine load had a significant effect on improving BSFC and BTE. Augmenting the proportion of canola oil and load can reduce HC emissions, but may increase NO_x emissions. However, the utilization of EGR technology can notably decrease NO_x emissions.

(4) Utilizing the response surface methodology for multi-objective optimization, the optimum operating conditions for the engine were found to be running at 100% load, with a biodiesel blend of 6.9% and an EGR rate of 7.7%. Following a comprehensive analysis, an ideal value of 0.656 was determined. At this configuration, the corresponding

values for BSFC, BTE, HC, and NO_x emissions were established as 282.62 g/(kW·h), 38.15%, 410.37 ppm, and 274.38 ppm, respectively.

Author Contributions: Conceptualization, Y.Y. and H.Z.; methodology, Y.Y.; software, S.G.; validation, Z.Z., Y.Y. and H.Z.; formal analysis, H.Z.; investigation, K.L.; resources, Y.Y.; data curation, H.Z.; writing—original draft preparation, Z.Z. and H.Z.; writing—review and editing, H.Z.; visualization, Z.Z.; supervision, K.L.; project administration, S.G.; funding acquisition, Z.Z. All authors have read and agreed to the published version of the manuscript.

Funding: This work is supported by the Guangxi Keb&D Program under the research grant AB22080085, and also supported by the Natural Science Foundation of Guangxi under the research grant 2024GXNSFAA010397.

Data Availability Statement: The original contributions presented in the study are included in the article, further inquiries can be directed to the corresponding author.

Acknowledgments: We would like to express our gratitude to Weizhu Li (Guangxi Yuchai Machine Parts Manufacturing Co., Ltd.) for his invaluable contribution to the conceptualisation, investigation and validation of the paper.

Conflicts of Interest: The authors declare that they have no conflict of interests regarding the publication of this paper.

Nomenclature

3D	Three-dimensional
CFD	Computational fluid dynamics
ANOVA	Analysis of variance
CPs	Cylinder pressures
B5	5% biodiesel + 95%diesel
D100	Pure diesel
B10	10% biodiesel + 90%diesel
EGR	Exhaust gas recirculation
B15	15% biodiesel + 85%diesel
FAME	Fatty acid methyl esters
B100	Pure biodiesel
HC	Hydrocarbon
BTE	Brake thermal efficiency
HRR	Heat release rate
BSFC	Brake specific fuel consumption
KH-RT	Kelvin Helmholtz model and Rayleigh Taylor
CI	Compression ignition
NO_x	Nitrogen oxides
CO	Carbon monoxide
RSM	Response surface methodology

References

1. Zhao, D.; Guan, Y. Characterizing Modal Exponential Behaviors of Self-excited Transverse and Longitudinal Combustion Instabilities. *Phys. Fluids* **2022**, *34*, 024109. [CrossRef]
2. Zhang, Z.; Zhong, W.; Mao, C.; Xu, Y.; Lu, K.; Ye, Y.; Guan, W.; Pan, M.; Tan, D. Multi-objective optimization of Fe-based SCR catalyst on the NO_x conversion efficiency for a diesel engine based on FGRA-ANN/RF. *Energy* **2024**, *294*, 130899. [CrossRef]
3. Fan, L.; Cheng, F.; Zhang, T.; Liu, G.; Yuan, J.; Mao, P. Visible-light photoredox-promoted desilylative allylation of a-silylamines: An efficient route to synthesis of homoallylic amines. *Tetrahedron Lett.* **2021**, *81*, 153357. [CrossRef]
4. Zhang, Z.; Wang, S.; Pan, M.; Lv, J.; Lu, K.; Ye, Y.; Tan, D. Utilization of Hydrogen-Diesel Blends for the Improvements of a Dual-Fuel Engine Based on the Improved Taguchi Methodology. *Energy* **2024**, *292*, 130474. [CrossRef]
5. Zhao, D.; Ephraim, J.; Gutmark, A. Reinecke, Mitigating self-excited flame pulsating and thermoacoustic oscillations using perforated liners. *Sci. Bull.* **2019**, *64*, 941–952. [CrossRef] [PubMed]
6. Liu, Y.; Li, S.J.; Chen, X.L.; Fan, L.L.; Li, X.Y.; Zhu, S.S.; Qu, L.B.; Yu, B. Mn(III)—Mediated Regioselective 6—endo—trig Radical Cyclization of o—Vinylaryl Isocyanides to Access 2—Functionalized Quinolines. *Adv. Synth. Catal.* **2019**, *362*, 688–694. [CrossRef]

7. Cai, T.; Zhao, D.; Gutmark, E. Overview of fundamental kinetic mechanisms and emission mitigation in ammonia combustion. *Chem. Eng. J.* **2023**, *458*, 141391. [CrossRef]
8. Cai, T.; Tang, A.; Li, C. Experimental and kinetic analyses on the flame dynamics and stabilization of ammonia/hydrogen-air mixtures in a micro-planar combustor. *Chem. Eng. J.* **2023**, *477*, 147038. [CrossRef]
9. Tan, D.; Dong, R.; Zhang, Z.; Zhang, B.; Jiang, F.; Ye, Y.; Li, D.; Liu, H. Multi-Objective Impact Mechanism on the Performance Characteristic for a Diesel Particulate Filter by RF-NSGA III-TOPSIS during Soot Loading. *Energy* **2024**, *286*, 129582. [CrossRef]
10. Zhang, Z.; E, J.; Deng, Y.; Pham, M.; Zuo, W.; Peng, Q.; Yin, Z. Effects of Fatty Acid Methyl Esters Proportion on Combustion and Emission Characteristics of a Biodiesel Fueled Marine Diesel Engine. *Energy Convers. Manag.* **2018**, *159*, 244–253. [CrossRef]
11. Cheng, F.; Fan, L.; Lv, Q.; Chen, X.; Yu, B. Alkyl radicals from diacyl peroxides: Metal-/base-/additive-free photocatalytic alkylation of N-heteroaromatics. *Green Chem* **2023**, *25*, 7971–7977. [CrossRef]
12. Zhang, Z.; Lv, J.; Xie, G.; Wang, S.; Ye, Y.; Huang, G.; Tan, D. Effect of assisted hydrogen on combustion and emission characteristics of a diesel engine fueled with biodiesel. *Energy* **2022**, *254*, 124269. [CrossRef]
13. Chang, Y.C.; Lee, W.J.; Wang, L.C.; Yang, H.H.; Cheng, M.T.; Lu, J.H.; Tsai, Y.I.; Young, L.H. Effects of Waste Cooking Oil-Based Biodiesel on the Toxic Organic Pollutant Emissions from a Diesel Engine. *Appl. Energy* **2014**, *113*, 631–638. [CrossRef]
14. Mourad, M.; Mahmoud, K.R.M.; NourEldeen, E.S.H. Improving Diesel Engine Performance and Emissions Characteristics Fuelled with Biodiesel. *Fuel* **2021**, *302*, 121097. [CrossRef]
15. Singh, B.; Korstad, J.; Sharma, Y.C. A Critical Review on Corrosion of Compression Ignition (CI) Engine Parts by Biodiesel and Biodiesel Blends and Its Inhibition. *Renew. Sustain. Energy Rev.* **2012**, *16*, 3401–3408. [CrossRef]
16. Manaf, I.S.A.; Embong, N.H.; Khazaai, S.N.M.; Rahim, M.H.A.; Yusoff, M.M.; Lee, K.T.; Maniam, G.P. A Review for Key Challenges of the Development of Biodiesel Industry. *Energy Convers. Manag.* **2019**, *185*, 508–517. [CrossRef]
17. Vélez Godiño, J.A.; Torres García, M.; Jiménez-Espadafor Aguilar, F.J. Experimental Analysis of Late Direct Injection Combustion Mode in a Compression-Ignition Engine Fuelled with Biodiesel/Diesel Blends. *Energy* **2022**, *239*, 121895. [CrossRef]
18. Karavalakis, G.; Johnson, K.C.; Hajbabaei, M.; Durbin, T.D. Application of Low-Level Biodiesel Blends on Heavy-Duty (Diesel) Engines: Feedstock Implications on NO and Particulate Emissions. *Fuel* **2016**, *181*, 259–268. [CrossRef]
19. Yoon, S.; Kim, M.; Kim, H.; Choi, N. Effects of Canola Oil Biodiesel Fuel Blends on Combustion, Performance, and Emissions Reduction in a Common Rail Diesel Engine. *Energies* **2014**, *7*, 8132–8149. [CrossRef]
20. Uyumaz, A.; Aydoğan, B.; Yılmaz, E.; Solmaz, H.; Aksoy, F.; Mutlu, İ.; İpci, D.; Calam, A. Experimental Investigation on the Combustion, Performance and Exhaust Emission Characteristics of Poppy Oil Biodiesel-Diesel Dual Fuel Combustion in a CI Engine. *Fuel* **2020**, *280*, 118588. [CrossRef]
21. Zhang, Z.; Ye, J.; Tan, D.; Feng, Z.; Luo, J.; Tan, Y.; Huang, Y. The Effects of Fe2O3 Based DOC and SCR Catalyst on the Combustion and Emission Characteristics of a Diesel Engine Fueled with Biodiesel. *Fuel* **2021**, *290*, 120039. [CrossRef]
22. Maiboom, A.; Tauzia, X.; Hétet, J.F. Experimental Study of Various Effects of Exhaust Gas Recirculation (EGR) on Combustion and Emissions of an Automotive Direct Injection Diesel Engine. *Energy* **2008**, *33*, 22–34. [CrossRef]
23. Chintala, V.; Subramanian, K.A. CFD Analysis on Effect of Localized In-Cylinder Temperature on Nitric Oxide (NO) Emission in a Compression Ignition Engine under Hydrogen-Diesel Dual-Fuel Mode. *Energy* **2016**, *116*, 470–488. [CrossRef]
24. Yokomura, H.; Kouketsu, S.; Kotooka, S.; Akao, Y. *Transient EGR Control for a Turbocharged Heavy Duty Diesel Engine*; SAE Technical Paper; SAE International: Warrendale, PA, USA, 2004; No. 2004–01–0120. [CrossRef]
25. Maurya, R.K.; Mishra, P. Parametric Investigation on Combustion and Emissions Characteristics of a Dual Fuel (Natural Gas Port Injection and Diesel Pilot Injection) Engine Using 0-D SRM and 3D CFD Approach. *Fuel* **2017**, *210*, 900–913. [CrossRef]
26. Rajesh Kumar, B.; Saravanan, S. Effect of Exhaust Gas Recirculation (EGR) on Performance and Emissions of a Constant Speed DI Diesel Engine Fueled with Pentanol/Diesel Blends. *Fuel* **2015**, *160*, 217–226. [CrossRef]
27. Dodge, L.G.; Simescu, S.; Neely, G.D.; Maymar, M.J.; Dickey, D.W.; Savonen, C.L. *Effect of Small Holes and High Injection Pressures on Diesel Engine Combustion*; SAE Technical Paper; SAE International: Warrendale, PA, USA, 2002; No. 2002–01–0494. [CrossRef]
28. Basha, S.A.; Gopal, K.R.; Jebaraj, S. A Review on Biodiesel Production, Combustion, Emissions and Performance. *Renew. Sustain. Energy Rev.* **2009**, *13*, 1628–1634. [CrossRef]
29. Han, Z.; Reitz, R.D. Turbulence Modeling of Internal Combustion Engines Using RNG κ-ε Models. *Combust. Sci. Technol.* **1995**, *106*, 267–295. [CrossRef]
30. Li, Y.; Huang, Y.; Luo, K.; Liang, M.; Lei, B. Development and Validation of an Improved Atomization Model for GDI Spray Simulations: Coupling Effects of Nozzle-Generated Turbulence and Aerodynamic Force. *Fuel* **2021**, *299*, 120871. [CrossRef]
31. Gao, S.; Ye, Y.; Tan, D.; Jia, G.; Zhang, B.; Liu, H.; Li, D.; Zhang, J.; Zhong, W.; Zhang, Z. Improvements of Performance and Emission Characteristics of a Diesel Engine Fueled with Diesel/PODE3/n-Butanol Blended Fuels by RSM-NSGA III in Plateau Environment. *Process Saf. Environ. Prot.* **2024**, *185*, 184–210. [CrossRef]
32. Pham, Q.; Park, S.; Agarwal, A.K.; Park, S. Review of Dual-Fuel Combustion in the Compression-Ignition Engine: Spray, Combustion, and Emission. *Energy* **2022**, *250*, 123778. [CrossRef]
33. Zhang, F.; Lei, F.; Feng, M.; Liao, G.; E, J. Investigation on the Effect of the Cooler Design on the Performance of Onboard Supercritical Carbon Dioxide Power Cycle for Hypersonic Vehicles. *Appl. Therm. Eng.* **2024**, *236*, 121854. [CrossRef]
34. Tan, D.; Meng, Y.; Tian, J.; Zhang, C.; Zhang, Z.; Yang, G.; Cui, S.; Hu, J.; Zhao, Z. Utilization of Renewable and Sustainable Diesel/Methanol/n-Butanol (DMB) Blends for Reducing the Engine Emissions in a Diesel Engine with Different Pre-Injection Strategies. *Energy* **2023**, *269*, 126785. [CrossRef]

35. Zhang, Z.; Lv, J.; Li, W.; Long, J.; Wang, S.; Tan, D.; Yin, Z. Performance and Emission Evaluation of a Marine Diesel Engine Fueled with Natural Gas Ignited by Biodiesel-Diesel Blended Fuel. *Energy* **2022**, *256*, 124662. [CrossRef]
36. Tan, D.; Wu, Y.; Lv, J.; Li, J.; Ou, X.; Meng, Y.; Lan, G.; Chen, Y.; Zhang, Z. Performance Optimization of a Diesel Engine Fueled with Hydrogen/Biodiesel with Water Addition Based on the Response Surface Methodology. *Energy* **2023**, *263*, 125869. [CrossRef]
37. Zhang, Z.; Li, J.; Tian, J.; Dong, R.; Zou, Z.; Gao, S.; Tan, D. Performance, Combustion and Emission Characteristics Investigations on a Diesel Engine Fueled with Diesel/Ethanol/n-Butanol Blends. *Energy* **2022**, *249*, 123733. [CrossRef]
38. Buyukkaya, E. Effects of Biodiesel on a DI Diesel Engine Performance, Emission and Combustion Characteristics. *Fuel* **2010**, *89*, 3099–3105. [CrossRef]
39. Daho, T.; Vaitilingom, G.; Ouiminga, S.K.; Piriou, B.; Zongo, A.S.; Ouoba, S.; Koulidiati, J. Influence of Engine Load and Fuel Droplet Size on Performance of a CI Engine Fueled with Cottonseed Oil and Its Blends with Diesel Fuel. *Appl. Energy* **2013**, *111*, 1046–1053. [CrossRef]
40. Mehta, R.N.; Chakraborty, M.; Parikh, P.A. Nanofuels: Combustion, Engine Performance and Emissions. *Fuel* **2014**, *120*, 91–97. [CrossRef]
41. Zhang, Z.; Liu, H.; Li, Y.; Ye, Y.; Tian, J.; Li, J.; Xu, Y.; Lv, J. Research and Optimization of Hydrogen Addition and EGR on the Combustion, Performance, and Emission of the Biodiesel-Hydrogen Dual-Fuel Engine with Different Loads Based on the RSM. *Heliyon* **2024**, *10*, e23389. [CrossRef]
42. Park, Y.; Bae, C. Experimental Study on the Effects of High/Low Pressure EGR Proportion in a Passenger Car Diesel Engine. *Appl. Energy* **2014**, *133*, 308–316. [CrossRef]
43. Hua, Y.; Wang, Z.; Li, R.; Liu, S.; Zhao, Y.; Qu, L.; Mei, D.; Lv, H. Experimental Study on Morphology, Nanostructure and Oxidation Reactivity of Particles in Diesel Engine with Exhaust Gas Recirculation (EGR) Burned with Different Alternative Fuels. *Energy* **2022**, *261*, 125249. [CrossRef]
44. Gatts, T.; Liu, S.; Liew, C.; Ralston, B.; Bell, C.; Li, H. An Experimental Investigation of Incomplete Combustion of Gaseous Fuels of a Heavy-Duty Diesel Engine Supplemented with Hydrogen and Natural Gas. *Int. J. Hydrogen Energy* **2012**, *37*, 7848–7859. [CrossRef]
45. Zhang, Z.; Tian, J.; Li, J.; Lv, J.; Wang, S.; Zhong, Y.; Dong, R.; Gao, S.; Cao, C.; Tan, D. Investigation on Combustion, Performance and Emission Characteristics of a Diesel Engine Fueled with Diesel/Alcohol/n-Butanol Blended Fuels. *Fuel* **2022**, *320*, 123975. [CrossRef]
46. Duan, X.; Xu, Z.; Sun, X.; Deng, B.; Liu, J. Effects of Injection Timing and EGR on Combustion and Emissions Characteristics of the Diesel Engine Fuelled with Acetone–Butanol–Ethanol/Diesel Blend Fuels. *Energy* **2021**, *231*, 121069. [CrossRef]
47. Labecki, L.; Ganippa, L.C. Effects of Injection Parameters and EGR on Combustion and Emission Characteristics of Rapeseed Oil and Its Blends in Diesel Engines. *Fuel* **2012**, *98*, 15–28. [CrossRef]
48. Saravanan, S.; Rao, G.L.N. Effect of EGR on Performance and Emission Characteristics of Diesel Engine at Advanced Injection Timing. *IJOGCT* **2014**, *7*, 335. [CrossRef]
49. Zhang, Z.; Tian, J.; Xie, G.; Li, J.; Xu, W.; Jiang, F.; Huang, Y.; Tan, D. Investigation on the Combustion and Emission Characteristics of Diesel Engine Fueled with Diesel/Methanol/n-Butanol Blends. *Fuel* **2022**, *314*, 123088. [CrossRef]
50. Shan, X.; Qian, Y.; Zhu, L.; Lu, X. Effects of EGR Rate and Hydrogen/Carbon Monoxide Ratio on Combustion and Emission Characteristics of Biogas/Diesel Dual Fuel Combustion Engine. *Fuel* **2016**, *181*, 1050–1057. [CrossRef]
51. Park, S.H.; Lee, C.S. Combustion Performance and Emission Reduction Characteristics of Automotive DME Engine System. *Prog. Energy Combust. Sci.* **2013**, *39*, 147–168. [CrossRef]
52. Wu, C.; Liang, K.; Sang, H.; Ye, Y.; Pan, M. A Low-Sample-Count, High-Precision Pareto Front Adaptive Sampling Algorithm Based on Multi-Criteria and Voronoi. *Soft Comput* **2023**, 1–17. [CrossRef]